# The Mesoscale and Microscale Structure and Organization of Clouds and Precipitation in Midlatitude Cyclones. XII: A Diagnostic Modeling Study of Precipitation Development in Narrow Cold-Frontal Rainbands

STEVEN A. RUTLEDGE[1] AND PETER V. HOBBS

*Atmospheric Sciences Department, University of Washington,[2] Seattle, WA 98195*

(Manuscript received 20 May 1983, in final form 6 August 1984)

ABSTRACT

The highest precipitation rates in midlatitude cyclones are often associated with the narrow cold-frontal rainband. In this paper the formation of precipitation in this type of rainband is analyzed with the aid of a diagnostic cloud model and field measurements.

Model results indicate that the high precipitation rates in narrow cold-frontal rainbands are associated with graupel. The graupel forms when ice particles, which originate in the stratiform cloud ahead of the rainband, grow rapidly by riming after entering the strong updraft (and hence a region of high liquid water content) associated with the rainband. When this source of input ice particles is not present the precipitation is somewhat weaker, but still mainly associated with graupel. In this case, the graupel forms as small, frozen drops grow by riming. The drops form in the updraft region due to the autoconversion of cloud water and they are frozen by collisions with small ice crystals. A series of sensitivity studies dealing with various model inputs and parameters are discussed. The model results agree reasonably well with field measurements.

## 1. Introduction

In previous papers in this series the structures of the various types of rainbands that occur in extratropical cyclones as they move onto the Pacific Coast of Washington State have been described (Hobbs *et al.*, 1980; Herzegh and Hobbs, 1980, 1981; Houze *et al.*, 1981; Hobbs and Persson, 1982; Wang *et al.*, 1983; Parsons and Hobbs, 1983a,b). Based on these field studies, which are part of the University of Washington's CYCLES (*CYCL*onic *E*xtratropical *S*torms) Project, conceptual models have been proposed for the primary cloud and precipitation processes operating in the rainbands (Hobbs, 1978; Matejka *et al.*, 1980). To test these conceptual models and to develop further insights into the mechanisms responsible for the formation of precipitation within the rainbands associated with extratropical cyclones, a series of numerical modeling studies have been undertaken. In a previous paper (Rutledge and Hobbs, 1983) we employed a diagnostic model to study warm-frontal rainbands. In the present paper we present the results of a similar modeling study for the narrow cold-frontal rainband.

The narrow cold-frontal rainband often contains the most intense precipitation within a cyclonic storm. Until recently this rainband was regarded as essentially a two-dimensional line feature, produced by strong convergence into the pressure trough at the leading edge of the cold airmass (e.g., Kessler and Wexler, 1960; Browning and Harrold, 1970). However, Hobbs (1978), James and Browning (1979) and Hobbs and Biswas (1979) showed that this rainband consists of a series of small, ellipsoidally-shaped precipitation "cores" that straddle the surface cold front and are aligned at a slight angle to the synoptic-scale cold front. Precipitation rates are high in the cores but markedly depressed in the "gap" regions between them.

Recently, Hobbs and Persson (1982) and Carbone (1982) have described detailed case studies of narrow cold-frontal rainbands. In both cases, a narrow intense updraft was observed directly above the location of the surface cold front. Immediately to the rear of this feature was a downdraft of similar width. In the case described by Hobbs and Persson, the magnitude of the updraft was 1–10 m $s^{-1}$; in the case reported by Carbone the updraft was >20 m $s^{-1}$. The downdrafts were generally less than half the magnitude of the updrafts.

The strong updrafts in narrow cold-frontal rainbands produce relatively high cloud liquid water contents, sometimes exceeding 1 g $m^{-3}$ (Matejka *et al.* 1980; Hobbs and Persson, 1982). CYCLES field studies indicate that the growth of ice particles by riming, which leads to graupel, is the dominant mechanism for particle growth in narrow cold-frontal

[1] Present affiliation: Department of Atmospheric Sciences, Oregon State University, Corvallis, OR 97331.

[2] Contribution No. *716*, Atmospheric Sciences Department, University of Washington.

rainbands (Hobbs, 1978; Matejka *et al.*, 1980; Hobbs and Persson, 1982). However, the mechanisms responsible for initiating the particles on which the graupel form is not apparent from the field studies.

The approach taken in this paper is similar to that used by Rutledge and Hobbs (1983, hereafter referred to as RH) in that microphysical model calculations are carried out in a prescribed air motion field, taken from a well-documented CYCLES case study. The results of the model calculations are then compared with measurements of other parameters from the same case study. The case study is that described by Hobbs and Persson.

## 2. Model description

The numerical model used in this study is similar to that described by RH, except that graupel is now included. This is a parameterized model, similar in many respects to the model discussed by Lin *et al.* (1983). The model is two dimensional in the $x$–$z$ plane, where $x$ is the horizontal distance perpendicular to the length of the narrow cold-frontal rainband and $z$ is the height coordinate. Model variables include temperature ($T$), and the mixing ratios of water vapor ($q_v$), cloud water ($q_c$), cloud ice ($q_i$), snow ($q_s$), rain ($q_r$) and graupel ($q_g$). The fields of cloud water and cloud ice advect with the airflow in both the horizontal and vertical directions. However, rain, snow and graupel, while moving with the horizontal wind, fall relative to the updraft. An important difference between the present model simulations and those described by RH is the grid spacing used. In the present simulations, the grid spacing is 600 m in the horizontal and 150 m in the vertical. These values were 4 km and 200 m, respectively, in RH.

### a. Parameterizations

We describe here only the parameterization used for the graupel field. Parameterizations for the other water continuity fields may be found in RH.

We assume that the particles comprising the graupel ($q_g$) field are distributed in size according to the relation:

$$N_{DG}dD_G = N_{0G}\exp(-\lambda_G D_G)dD_G, \tag{1}$$

where $N_{DG}dD_G$ ($m^{-3}$) is the number of graupel particles per cubic meter of air with diameters between $D_G$ and $D_G + dD_G$, $N_{0G}$ ($m^{-4}$) the intercept value, and $\lambda_G$ ($m^{-1}$) the slope of the distribution, which is given by

$$\lambda_G = \left(\frac{\pi\rho_G N_{0G}}{\rho q_g}\right)^{0.25}. \tag{2}$$

In this study we set $N_{0G} = 4 \times 10^6$ $m^{-4}$ based on the study by Houze *et al.* (1979).

### b. Continuity equations

The continuity equation for graupel ($q_g$) is

$$\frac{\partial q_g}{\partial t} = -u\frac{\partial q_g}{\partial x} - (w - \bar{V})\frac{\partial q_g}{\partial z} - \frac{q_g}{\rho}\frac{\partial}{\partial z}(\rho\bar{V}) + \frac{S_0}{\rho}, \tag{3}$$

where $\bar{V}$ is the mass-weighted fallspeed of graupel and $S_0$ represents the sources and sinks of graupel (defined in Appendix A).

### c. Cloud processes

The microphysical processes included in the narrow cold-frontal rainband model are indicated schematically in Fig. 1. Since many of the processes have been discussed by RH they will not be described again here. Only those terms required for the initiation, and the subsequent growth (or destruction) of graupel, will be discussed. We will employ the acronyms used by Lin *et al.* to represent various microphysical processes.

#### 1) MECHANISMS FOR THE INITIATION OF GRAUPEL

Graupel can be initiated in the model by three mechanisms: collisions between rain and cloud ice, collisions between rain and snow, and collisions between snow and cloud water (riming). The mixing ratios of cloud water, rain and snow are denoted by the symbols $q_c$, $q_r$ and $q_s$, respectively. When a raindrop collides with cloud ice at $T < 0$°C, the freezing of the drop is assumed to initiate a graupel particle provided $q_r > 0.1$ g $kg^{-1}$. If the latter requirement is not met, this freezing process becomes a source for snow. When graupel is initiated by this mechanism, both rain and cloud ice are transferred to the graupel category. Hence, two terms are required, PIACR which gives the rate that rain is transferred to either snow or graupel, and PRACI which computes the associated loss term for cloud ice. This combined process is represented by P*RACI in Fig. 1.

Collisions between rain and snow at $T < 0$°C are another possible source of graupel. For graupel to be initiated by this process, both $q_r$ and $q_s$ must exceed 0.1 g $kg^{-1}$. If these conditions are not met, collisions between snow and rain are assumed to result in an increase in snow by riming. This process for forming graupel can be thought of as originating by drop freezing (for instance, when large drops collide with small snow particles) or by the riming of snow particles (when large snow particles collide with relatively small raindrops). Again two terms are required, PSACR which gives the rate that rain is removed due to accretion by snow, and PRACS represents the associated loss term for snow. These processes are represented by P*SACR in Fig. 1.

The two graupel initiation mechanisms discussed above, and the thresholds that must be met before initiation can take place, are identical to those given

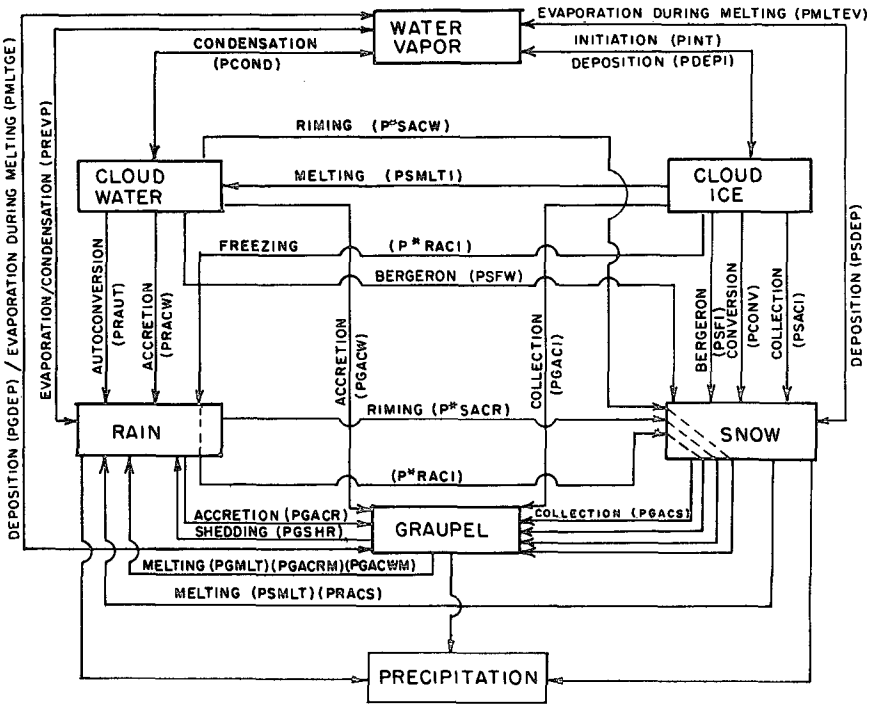


FIG. 1. Schematic depicting the cloud and precipitation processes included in the model for the study of narrow cold-frontal rainbands.

by Lin *et al.* (1983). However, the present model includes a third graupel initiation mechanism. If at a particular gridpoint $q_s$ and $q_c$ are >0.1 g kg$^{-1}$ and >0.5 g kg$^{-1}$, respectively, riming is considered to take place at a large enough rate that graupel forms, hence both snow and cloud water are transferred to the graupel category. If these thresholds are not met, snow grows by the accretion of cloud water and graupel is not initiated. Like the above two processes two terms are again required for this graupel initiation mechanism (represented collectively by P*SACW in Fig. 1). PWACS computes the rate that snow is transferred to graupel due to riming, and PSACW represents the associated loss term for cloud water.

Lin *et al.* allowed graupel to be initiated by collisions between snow particles, using an autoconversion-like parameterization. A threshold mixing ratio for snow of 0.6 g kg$^{-1}$ was used. We do not consider this process to be an important graupel initiation mechanism. Graupel initiation mechanisms in our model are due only to those processes that involve collisions between liquid water and ice.

The threshold values that must be exceeded before graupel can be initiated by the mechanisms discussed above are somewhat arbitrary, as they are not readily derived from field measurements or theoretical considerations. This is a problem that is faced by all parameterized models of this type. The sensitivity of the model to the assumed threshold values will be examined in a later section.

### 2) SOURCES AND SINKS FOR GRAUPEL

The growth of graupel when $T < 0$°C can occur by the accretion of cloud water (PGACW) or rainwater (PGACR). The collection of cloud ice (PGACI) or snow (PGACS) provide additional sources for graupel. When $T < 0$°C and the air is supersaturated with respect to ice, graupel is allowed to grow by vapor deposition (PGDEP).

When $T \geq 0$°C the following processes are sinks for graupel. The melting of graupel is represented by PGMLT. Enhanced melting of graupel can occur when graupel collects either cloud water or rainwater below the freezing level (PGACWM and PGACRM, respectively). Liquid water may evaporate from the surface of graupel when it melts in an environment below water saturation (PMLTGE). Since the cloud water and rainwater accreted by graupel when $T \geq 0$°C cannot be frozen, it must be shed. For this process we adopt the formulation of Lin *et al.* (1983) and assume the rate at which the accreted water is shed (PGSHR) is equal to the rate at which both cloud and rainwater are collected (PGACW + PGACR). The water that is shed from the graupel particle is a source for rainwater. The forms of the parameterizations for the above processes are given in Appendix A. A complete list of symbols is given in Appendix B.

An additional microphysical process included in the present model that is not described in RH is the

production of snow by the Bergeron process. For this process we use the formulation of Lin *et al.*, which includes both the transfer of cloud ice to snow (PSFI) and the transfer of cloud water to snow (PSFW).

### *d. Computation of radar reflectivities*

A valuable check on the model is provided by comparing the computed and measured radar reflectivities. For rain, a rearranged version of the $Z$–$R$ relation given by Marshall and Palmer (1948) is used:

$$\mathrm{dB}(Z_R) = 42.2 + 16.8 \log_{10} M_R, \qquad (4)$$

where $M_R$ (g m$^{-3}$) is given by $10^3\ \rho q_r$.

The radar reflectivity due to ice particles (both snow and graupel) is computed when $T < 0°\mathrm{C}$ using a rearranged version of the relationship given by Herzegh and Hobbs (1980):

$$\mathrm{dB}(Z_I) = 34.7 + 16.5 \log_{10}(M_S + M_G), \qquad (5)$$

where $\mathrm{dB}(Z_I)$ is the reflectivity from both snow and graupel, $M_S = 10^3\ \rho q_s$ and $M_G = 10^3\ \rho q_g$. Since (5) assumes scattering from ice, whereas the reflectivities derived from the radar measurements assume water scatterers, 6.7 dB($Z$) must be added to (5) before comparing with field data.

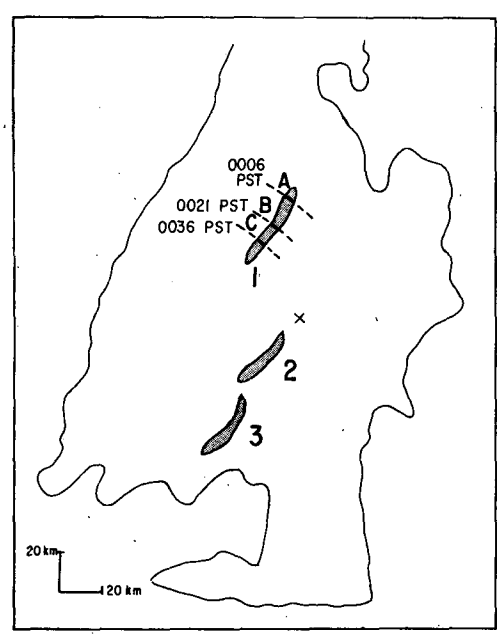


FIG. 2. Radar reflectivity display at an elevation angle of 0° at 0104 PST on 27 February 1979. The radar (NCAR's CP-3) was located at Pt. Brown (cross) on the Washington coast. The shaded ("core") regions, labelled 1–3, lie along the surface cold front and have reflectivities ≥ 40 dB($Z$). The surrounding contour encloses reflectivities of ≥20 dB($Z$). The dashed lines (A–C) through core 1 denote various vertical cuts along which the airflow pattern was analyzed.

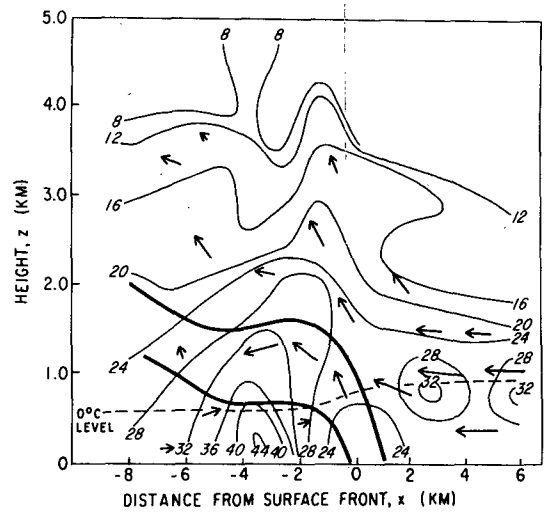


FIG. 3. Vertical cross section through and perpendicular to the narrow cold-frontal rainband on 27 February 1979. Arrows denote the air motion pattern relative to the rainband, which was moving from left to right at a speed of 12.5 m s$^{-1}$. Radar reflectivities in the plane are indicated by the light contours [labeled in dB($Z$)]. The windshift zone associated with the cold-frontal passage was located between the two heavy lines. (Adapted from Hobbs and Persson, 1982).

## 3. Field data and design of the modeling studies

In the narrow cold-frontal rainband studies described by Hobbs *et al.* (1980), Hobbs and Persson (1982) and Matejka *et al.* (1980), the rainband was embedded within a broader region of lighter precipitation. Shown in Fig. 2 is a radar reflectivity scan of the narrow cold-frontal rainband described in the Hobbs and Persson case study (the rainband to be modeled in this paper). This rainband (indicated by the high reflectivity cores) was clearly embedded within a broader region of lighter precipitation indicated by the weaker radar reflectivity.

Shown in Fig. 3 is a composite of the radar reflectivity and air motion patterns measured in this cold front. The updraft region associated with the rainband is located at $x = 0$. Examination of the radar echo structure reveals an area immediately ahead of the rainband that is characterized by horizontally-oriented reflectivity contours, typical of stratiform precipitation. Portions of a radar bright band are also present near the 1 km level. At Point Brown, on the Washington coast, light and continuous rain was recorded before, and immediately prior to, the passage of the narrow cold-frontal rainband; the rainfall rate suddenly increased with the passage of the rainband.

The airflow depicted in Fig. 3 is characterized by strong low-level flow into the leading edge of the narrow cold-frontal rainband between the surface and the 1.7 km level. Since the 0°C level was near the 700 m level, it appears likely that falling ice particles

(or the drops that formed from them upon melting) could have been swept into the narrow cold-frontal rainband and become incorporated into the rainband circulation. In this way, ice particles produced in the stratiform clouds ahead of the narrow cold-frontal rainband could have influenced the production of precipitation within the rainband. Browning and Harrold (1970) deduced from field studies, and Jonas and Tabony (1973) deduced from simple modeling studies, that the influx of ice particles into a narrow cold-frontal rainband was crucial to the formation of graupel in the shallow (~3 km deep) updraft.

The airborne data presented by Hobbs and Persson (1982), as well as by Matejka *et al.* (1980), supports the view that ice particles from surrounding stratiform clouds can enter the updraft region of narrow cold-frontal rainbands. For example, in the case described by Hobbs and Persson, graupel, as well as heavily rimed large ice crystals and aggregates, were present in the updraft region. It seems quite unlikely that the large ice particles and aggregates could have originated within the relatively warm, shallow updraft region; more likely, they originated in the surrounding stratiform clouds.

In view of these considerations our model simulations are designed in the following way. We consider the primary simulation to be that where the airflow pattern associated with the narrow cold-frontal rainband is embedded within a broad region of light precipitation. This will be referred to as the *embedded* simulation. Comparisons are then made between this simulation and field data presented in the Hobbs and Persson case study. After this we discuss a series of model sensitivity studies, the first one of which considers precipitation production within the rainband in the absence of any surrounding precipitation.

## 4. Input conditions for the model

The input data required for the numerical model simulations are taken from the well documented case study described by Hobbs and Persson. A sounding launched from Point Brown on the Washington coast, just 30 min prior to the passage of the rainband, provides the required model input data for temperature, pressure and water vapor mixing ratio. The horizontal and vertical wind fields were computed by Hobbs and Persson from Doppler radar data and by applying the continuity equation in two dimensions (within the plane perpendicular to the narrow cold-frontal rainband). The vertical motion was assumed to vanish at the lower boundary. The accuracy of the vertical motion pattern computed by this method is within a factor of two of the actual vertical motion pattern (the main source of error being the two-dimensional assumption, i.e., the divergence along the rainband core is small compared to the cross-core divergence). The horizontal wind relative to the rainband is shown in Fig. 4a. This field is characterized

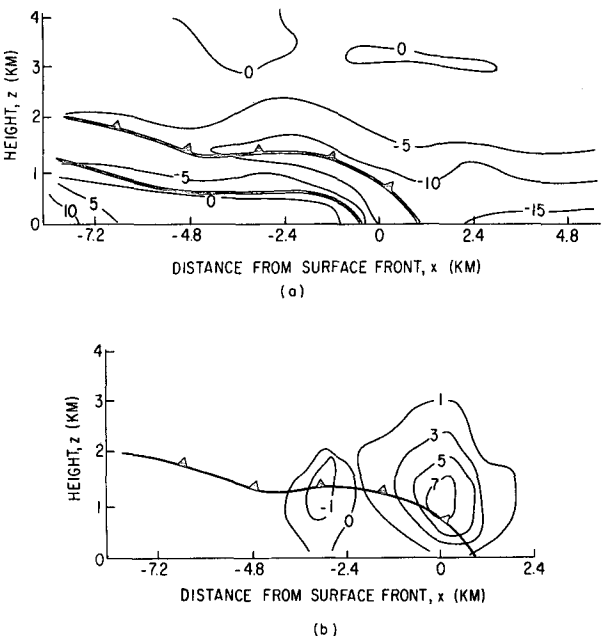


FIG. 4. Horizontal and vertical wind profiles used in the model simulations. (a) Horizontal wind speeds (m $s^{-1}$) relative to the rainband. Negative values denote winds moving from right to left and positive values denote winds moving from left to right. The windshift zone associated with the cold-frontal passage was located between the two heavy lines. (b) Vertical wind speeds (m $s^{-1}$); positive and negative values indicate updrafts and downdrafts, respectively. (From Hobbs and Persson, 1982).

by strong low-level inflow ahead of the cold front at the surface. Weaker flow is present behind the surface front. There is very little relative flow above 2 km. The updraft and downdraft regions are shown in Fig. 4b. Peak updraft speeds, in excess of 7 m $s^{-1}$, occur immediately above the surface front. The downdraft intensity has a maximum value of only 1 m $s^{-1}$.

The air motion pattern perpendicular to the rainband derived by Hobbs and Persson represents the airflow at a particular time (0036 PST) and at a specific location (represented by the dashed line C in Fig. 2) through one of the precipitation cores along the narrow cold-frontal rainband. In our model calculations we assume that the growth of precipitation occurs within a two-dimensional ($x$–$z$) plane oriented normal to the length of the narrow cold-frontal rainband. However, examination of the wind structure (from Doppler radar data) in the vicinity of the narrow cold-frontal rainband indicates that it is unlikely that a particle is confined to a single two-dimensional vertical plane. Rather, strong flow along the length of the rainband transports particles in this direction as they cross the rainband. Thus, the actual horizontal distance that a particle travels would be greater than that obtained by projection onto the $x$–$z$ plane. However, provided the air motion pattern in the $x$–$z$ plane is similar along any vertical cross

section normal to the rainband, particle growth can be computed as if it occurred within a single plane. This is because the growth rates of particles comprising the various fields included in the model are dependent only on time.

To check the uniformity of the flow along the rainband, air motions were computed in two additional perpendicular cross sections (indicated by the dashed lines A and B in Fig. 2). The airflow patterns in the vertical cross sections through lines A and B were similar to the flow shown in Fig. 4. Both were characterized by strong low-level inflow that decreased sharply with height. The vertical velocity pattern consisted of a strong updraft, followed by a less intense downdraft of similar horizontal width. The magnitudes of the computed vertical velocities were also very similar. The similarities in the air motion patterns along cuts A–C permit the use of the two-dimensional model to describe the growth of particles that actually move in three dimensions through the narrow cold-frontal rainband.

## 5. Model results for the embedded case

In this section we discuss model results for the embedded case, that is, the airflow pattern shown in Fig. 4 is embedded within a broad region of light precipitation. This broad region of stratiform precipitation is parameterized by a vertical line source of snow, constant with time, located approximately 5 km ahead of the updraft region. The snow mixing ratio in this vertical profile is determined by applying (5), with $M_G = 0$, to the observed radar reflectivity data in this region (Fig. 3). The precipitation particles in this region were identified by Hobbs and Persson as consisting of large ice crystals and aggregates with no obvious signs of riming, typical of stratiform precipitation.

Figure 5 is a schematic showing the values of the input snow ($q_{s0}$) ranging from 0.05 g kg$^{-1}$ at 4 km to

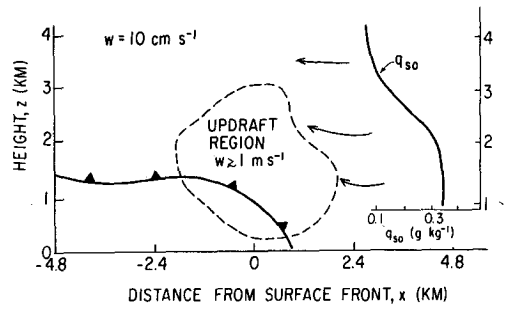


FIG. 5. Schematic showing the input conditions used in modeling the embedded case. Shown are the values of the input snow ($q_{s0}$) from the stratiform region ahead of the cold front and the trajectories (500 s displacements) of these particles. The vertical line source of snow from the stratiform cloud is input into the model at $x = 5$ km. Outside of the indicated updraft–downdraft region a constant updraft of 10 cm s$^{-1}$ was assumed.

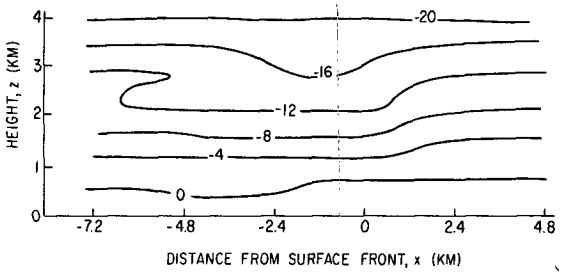


FIG. 6. The temperature field (°C) for the embedded simulation. The horizontal axis denotes distances ahead of and behind the location of the surface cold front. The vertical axis represents height above the ocean surface.

0.34 g kg$^{-1}$ at 700 m, computed by the method discussed above. Also shown in this figure are the trajectories of the input snow for 500 s displacements. It is clear that snow particles falling from above the 1 km level would have encountered the updraft region associated with the narrow cold-frontal rainband. However, snow particles falling from the 1 km level and below would not have been swept into the updraft region; instead, they would have melted and fallen to the surface ahead of the rainband. (The 0°C level was located approximately 700 m above the surface in this region.) To simulate the slow ascent in stratiform clouds we allow a weak updraft of 10 cm s$^{-1}$ to be present outside the updraft–downdraft region associated with the rainband. The model simulation was conducted by activating simultaneously the air motion pattern and the vertical line source of snow and proceeding until a steady state was achieved. This occurred after 3000 s of integration time.

Shown in Fig. 6 is the model derived temperature field in the $x$–$z$ cross-sectional plane for the embedded simulation. Due to adiabatic expansion of the rising air, the updraft region is characterized by lower temperatures than the inflow air. Warming due to the release of latent heat when condensation occurs is not of sufficient magnitude to offset this cooling. The small perturbation in the height of the 0°C isotherm between about $x = -1.2$ and $-5.4$ km is due to two factors, the melting of precipitation ice in this region and the presence of a downdraft. Heating in the updraft region resulting from ice deposition processes was small due to the low content of cloud ice. The reasons for the rather low production of cloud ice in the updraft region will be discussed later.

It should be emphasized that the temperature field produced by the model is a diagnostic quantity since the temperature field is not allowed to interact with the air motion field in a true dynamical sense. This is the reason for the rather sharp temperature gradient at the leading edge of the updraft region where a sharp horizontal gradient in the vertical velocity field is located.

The cooling produced by the strong vertical motions in the updraft region results in relatively large rates

of water vapor condensation (Fig. 7a). Regions of positive values of PCOND (condensation) and negative values (evaporation) coincide with centers of upward and downward motion, respectively. The peak condensation rate is $1.5 \times 10^{-2}$ g kg$^{-1}$ s$^{-1}$ and is located at the 1 km level, immediately above the surface front. Condensation rates reach maximum values at low levels, due to the strong dependence of the saturation mixing ratio on temperature and pressure and also because the maximum vertical velocities occur at low levels.

As expected, the distribution of cloud water (Fig. 7b) follows that of the condensation field. Cloud liquid water contents reach peak values of 0.9 g kg$^{-1}$ near the location of the maximum vertical velocity. The average observed liquid water contents in the updraft region were 0.7–1.5 g kg$^{-1}$. Because of the fairly high temperatures in the updraft region, and hence low ice nucleus concentrations (everywhere <0.1 L$^{-1}$ in the updraft region), the cloud ice field was small (<$10^{-3}$ g kg$^{-1}$).

The snow mixing ratio ($q_s$) for the embedded simulation is shown in Fig. 8. Ahead of the surface cold front (or strong updraft region) the snow content is simply due to the line source of snow at $x = 5$ km. The snow content remains relatively unchanged until just prior to the location of the cold front at the surface. Ahead of the surface cold front there is no

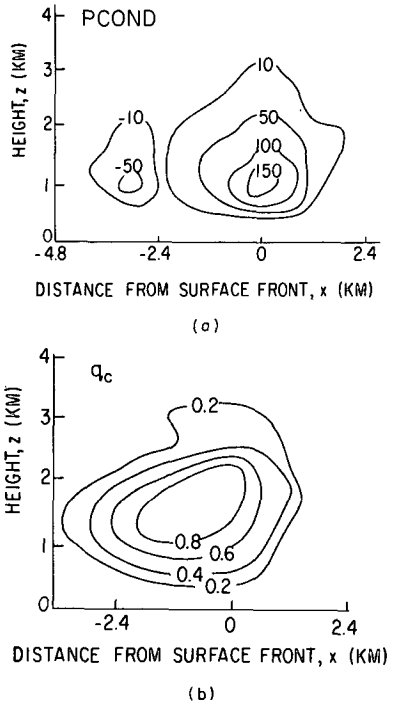


FIG. 7. Model results in the embedded simulation for (a) Condensation rate (PCOND), in units of $10^{-4}$ g kg$^{-1}$ s$^{-1}$. Negative values denote regions of evaporation. (b) Cloud water mixing ratio ($q_c$) in units of g kg$^{-1}$.

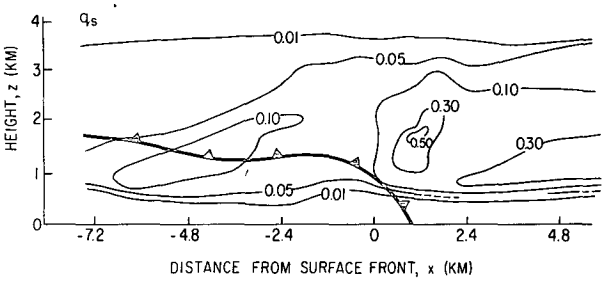


FIG. 8. The snow mixing ratio ($q_s$) in the embedded simulation. Units are g kg$^{-1}$. The cold front is indicated by the usual symbol.

cloud water available for the snow to grow by riming, and depositional growth is relatively slow at these temperatures. As the input snow encounters the cloud water content in the updraft region, riming occurs, leading to peak values of $q_s$ of 0.5 g kg$^{-1}$. However, beyond this point, the snow content rapidly decreases to <0.1 g kg$^{-1}$. This is a result of graupel initiation via the riming mechanism (P*SACW). Recall that graupel can form in the model by the riming of snow when $q_c > 0.5$ g kg$^{-1}$ and $q_s > 0.1$ g kg$^{-1}$ simultaneously. Since these threshold criteria are met at $0 \leq x \leq 1$ km, both snow and cloud water are transferred to the graupel category in this region. Initiation mechanisms for snow, including the conversion of cloud ice (PCONV), the Bergeron process (PSFW, PSFI) and raindrop freezing (PRACI, PIACR), were all relatively small and could not sustain the snow content in the updraft region. The secondary maximum in the $q_s$ field between $x = -2.4$ and $x = -7.2$ km is due to snow growing by riming. The snow particles in this region were either initiated in the updraft region by the above mechanisms or had origins in the stratiform clouds ahead of the surface front and traversed the updraft region without converting to graupel.

The graupel field ($q_g$) in this simulation is shown in Fig. 9. The graupel content is characterized by a relatively large mixing ratio near the top of the updraft region, with a peak value of 5 g kg$^{-1}$. This is an "accumulation level" for graupel in the model. The graupel is carried upward until its mass-weighted

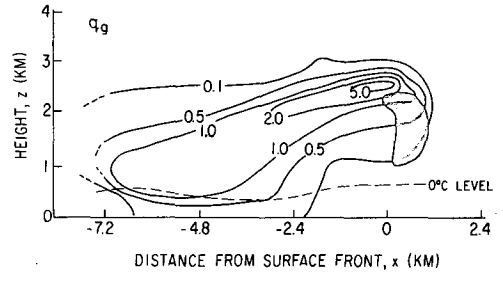


FIG. 9. The graupel mixing ratio ($q_g$) in the embedded simulation. The hatched area denotes the region where graupel is initiated by snow accreting cloud water. Units are g kg$^{-1}$.

fallspeed is equal to the updraft velocity. At this point, the graupel begins to fall relative to the updraft. Because of the weak horizontal flow at this level (Fig. 4a), horizontal transport is small and graupel accumulates. After exiting the top of the updraft the graupel moves rearward and falls toward the surface, hence the presence of the tilted graupel shaft indicated by the 1.0 g kg$^{-1}$ contour in Fig. 9.

The hatched region in Fig. 9 corresponds to the region where graupel is initiated by the riming mechanism. Hence, both cloud water (PSACW $\sim 10^{-3}$ g kg$^{-1}$ s$^{-1}$) and snow (PWACS $\sim 10^{-2}$ g kg$^{-1}$ s$^{-1}$) are transferred to the graupel category here. Thus this graupel initiation mechanism is confined to the leading edge of the updraft region. The two other graupel initiation mechanisms included in the model, collisions between rain and snow (provided both $q_r$ and $q_s > 0.1$ g kg$^{-1}$) or collisions between rain and cloud ice (provided $q_r > 0.1$ g kg$^{-1}$ and $q_i > 0$), were not activated. The rain water mixing ratio $q_r$ is shown in Fig. 10. Clearly the $q_r$ values are well below the threshold value of 0.1 g kg$^{-1}$ required for rain to participate in the initiation of graupel. The rain content (initiated by autoconversion) remained small due to the presence of graupel and snow that provided sinks for rain via accretion (PGACR, PSACR). The maximum values of $q_r$ at the surface near $x = -4.8$ km are associated with the melting of graupel as the heavy graupel precipitation shaft (Fig. 9) passes through the 0°C level.

We now examine the growth mechanisms for graupel after it has been initiated by the riming of snow. The most significant growth mechanisms are shown in Fig. 11. Of these, graupel accreting cloud water (PGACW) is by far the most important (Fig. 11a). Graupel grows primarily in the updraft region where the cloud water contents are the largest. The accretion of rain contributes somewhat to the graupel content (PGACR) and is confined to the lower portion of the updraft region (Fig. 11b). Near the top of the updraft region, vapor deposition contributes to the graupel mass (PGDEP) but only in a minor way (Fig. 11c). Growth terms of even lesser importance are the collection of snow (PGACS), which approached values of $10^{-5}$ g kg$^{-1}$ s$^{-1}$ only in a limited area near the top of the updraft region, and the collection of cloud ice by graupel (PGACI), which was $<10^{-9}$ g kg$^{-1}$ s$^{-1}$.

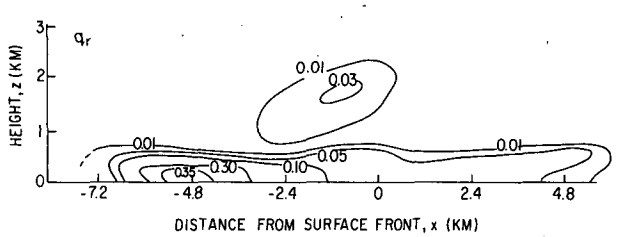


FIG. 10. The rain mixing ratio ($q_r$) in the embedded simulation. Units are g kg$^{-1}$.

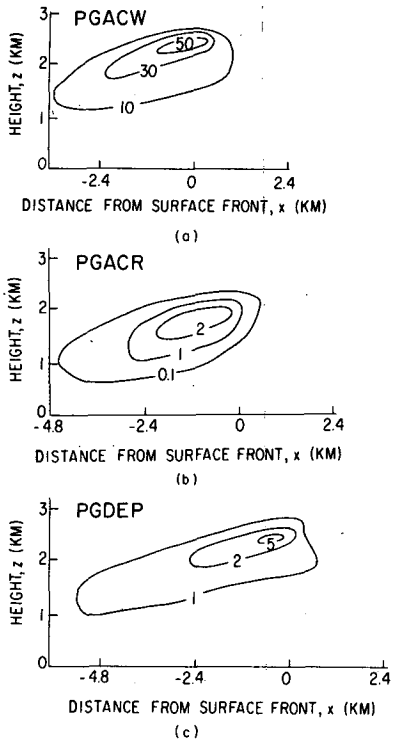


FIG. 11. Growth rates of graupel in the embedded simulation: (a) by accretion of cloud water (PGACW), (b) by accretion of rain (PGACR), and (c) by deposition of vapor (PGDEP). Units are $10^{-4}$ g kg$^{-1}$ s$^{-1}$.

The above model results indicate that snow particles originating in the stratiform clouds ahead of the narrow cold-frontal rainband grew rapidly by riming as they entered the updraft region, thus initiating graupel. The subsequent growth of graupel was dominated by the accretion of cloud water. This agrees with Hobbs and Persson's conclusions, which were based on the field observations.

The cloud water field is crucial to the development and continued growth of graupel through accretion. It is therefore instructive to examine the production terms for cloud water at a series of constant heights through the narrow cold-frontal rainband. By doing this, we can obtain vertical profiles of the source (condensation) and sinks (evaporation, autoconversion and accretion) of cloud water.

The results of this analysis are shown in Figs. 12a–d. Shown in Fig. 12a are the values of the source and sink terms for cloud water at the 1 km level. (An additional sink term for cloud water (PSFW) is not included in this analysis since it was generally quite small.) Clearly this is a production level for cloud water due to the condensation of water vapor.

At the 2 km level there is still a net production of cloud water, again resulting from strong condensation (Fig. 12b). However, as the graupel content begins to increase, the rate at which cloud water is removed by colliding with graupel at 2 km is significantly larger

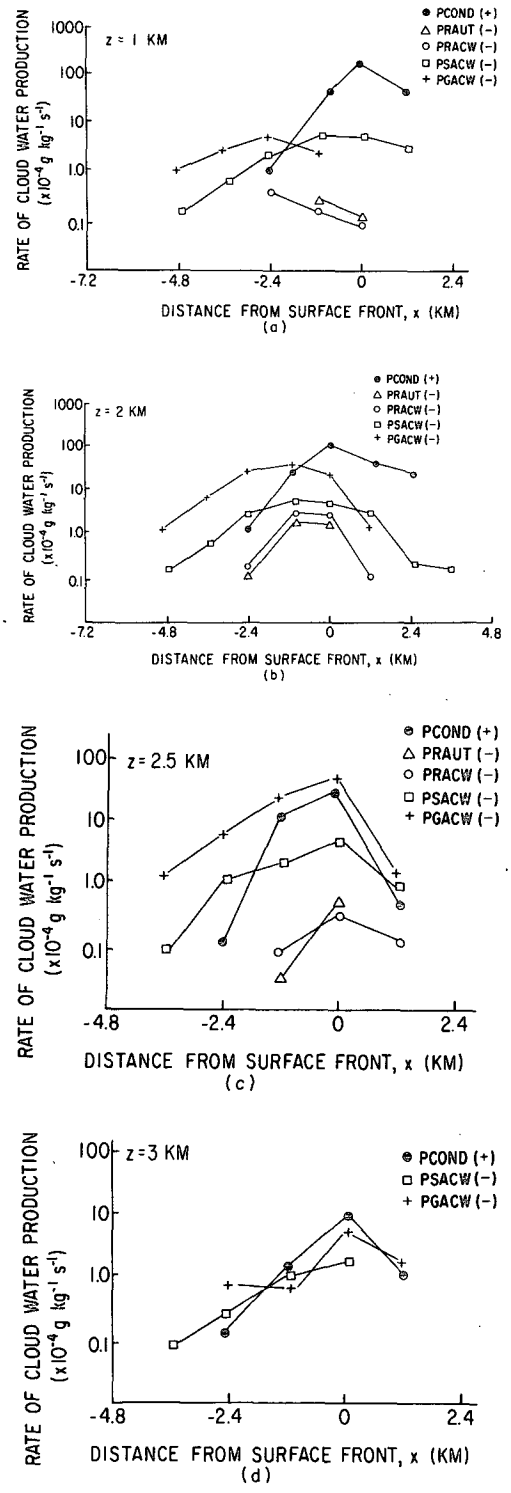


FIG. 12. The source and sinks of cloud water in the embedded simulation at various levels in the narrow cold-frontal rainband: (a) 1 km level, (b) 2 km level, (c) 2.5 km level, and (d) 3 km level.

than that at the 1 km level. The formation of rain in the updraft region by autoconversion (PRAUT) and collection (PRACW) is also somewhat larger at this level. The removal of cloud water between $x = 1.2$ and $x = -2.4$ km is due primarily to graupel moving up through the updraft region. Cloud water is removed between $x = -2.4$ and $x = -4.8$ km by graupel falling downward from the 2 km level and above.

At the 2.5 km level the rate at which cloud water is removed due to accretion by graupel is now larger than the production rate of cloud water by condensation (Fig. 12c). Hence, in contrast to lower levels, cloud water is removed more rapidly than it is produced. The accretion term (PGACW) is quite large because of the large graupel content at this level (Fig. 9). The condensation rate (PCOND) decreases at this level due to the rapid decrease with height of the updraft velocity. The production of rain by autoconversion and collection is also less at 2.5 than at 2 km.

At 3 km the magnitudes of the source and sinks for cloud water decrease sharply (Fig. 12d). The condensation rate is now an order of magnitude less than at 1 and 2 km. The accretion of cloud water by graupel (PGACW) is also less by nearly an order of magnitude. The condensation rate is small because the strong updraft generated by the surface convergence does not extend to this level. Condensation rates are also lower because of the strong decrease in the saturation mixing ratio with height. PGACW is small because the graupel has begun to fall to the surface below this level. The autoconversion of cloud water to rain (PRAUT) and the collection of cloud water by rain (PRACW) are now both zero.

The above analysis indicates the importance of the low-level organization of the narrow cold-frontal rainband. The bulk of the condensation that produces the relatively large values of cloud water is confined to the 2 km level and below. Nearly all the accretional growth of graupel is located below 2.5 km. Both of the above processes are closely linked to the shallow updraft region. The updraft is confined to low levels, since it is forced by strong convergence at the surface cold front, which occurs within a relatively shallow layer of conditionally unstable air.

The precipitation rate in the $x$–$z$ cross section for the embedded simulation is shown in Fig. 13. Three zones, characterized by widely different precipitation rates, are readily identifiable.

Ahead of the updraft region, for $x > 1.2$ km, the

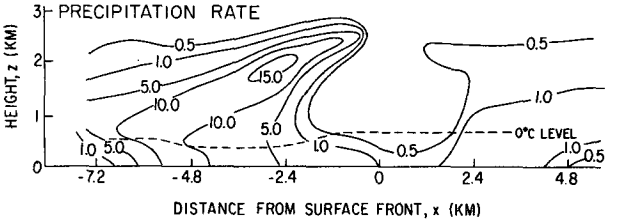


FIG. 13. Precipitation rates in the embedded simulation. Above the 0°C level, the rate is the melted equivalent. Units are mm $h^{-1}$.

precipitation rate is fairly uniform, with surface rates $\sim 1$ mm h$^{-1}$. The precipitation in this region is due to the input snow ($q_{s0}$). Above the 0°C level, the precipitation rate is in the form of snow that arrives at the surface as rain after undergoing melting. The contours of the precipitation rate are oriented horizontally, which is characteristic of stratiform precipitation.

The second precipitation zone is located between $x = 1.2$ and $x = -1.2$ km. This region largely encloses the strong updrafts associated with the narrow cold-frontal rainband (see Fig. 4b). Within this zone the precipitation rates above and below the 0°C level are nearly zero. This is because the strong updrafts in this region prevent particles from falling to the surface. The minimum surface precipitation rate is virtually co-located with the surface front.

The third precipitation zone is located where $x \leq -1.2$ km. Here the precipitation rate increases rapidly. The peak in the surface precipitation rate, located 5 km to the rear of the surface front, is 12.3 mm h$^{-1}$. The precipitation above the 0°C level in this region is dominated by graupel; the contributions from snow ($\sim$0.3 mm h$^{-1}$) and rain ($\sim$0.1 mm h$^{-1}$) are comparatively small. Once graupel passes the 0°C level, rapid melting occurs. This melting is due not only to the exposure of graupel to warmer air (PGMLT) but also to accretion (PGACRM). The melting is such that the peak precipitation rate at the surface was only 3.1 mm h$^{-1}$ in the form of graupel with the remaining 9.2 mm h$^{-1}$ as rain.

The variations in the surface precipitation rate in this simulation agree well with field studies in which three precipitation zones have been identified during the passage of a narrow cold-frontal rainband (Matejka *et al.*, 1980). The precipitation rate prior to the passage of a cold front is fairly steady. Coincident with the frontal passage (at the time of the windshift and pressure check), when the strong updraft is overhead, precipitation virtually ceases; Matejka *et al.* (1980) inferred from field observations that at this time the precipitation particles are suspended aloft. Several minutes later the heaviest precipitation occurs and lasts for $\sim$5 min. This burst of heavy precipitation

TABLE 1. Comparisons between the precipitation rates (mm h$^{-1}$) for the embedded simulation and field measurements.

| Model results | | Measurements | |
|---|---|---|---|
| Peak* | Average** | Peak | Average |
| 12.3 | 9.0 | 18.0† | 8.0§ |

* Maximum precipitation rate at the surface.

** Average precipitation rate at the surface between $x = -2.4$ and $x = -7.2$ km during the passage of the narrow cold-frontal rainband.

† 2 min average precipitation rate from core 2.

§ 10 min average precipitation rate from core 2.

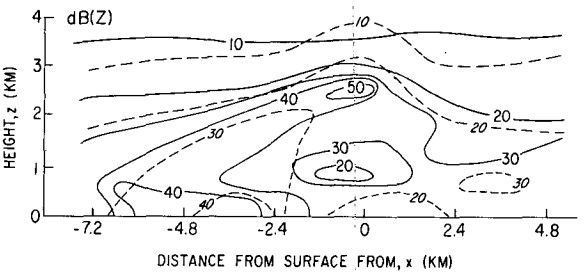


FIG. 14. Radar reflectivities [in dB($Z$)] for the embedded simulation (solid lines). Also shown are the measured values (dashed lines) taken from Hobbs and Persson (1982).

usually coincides with the fall in temperature (Hobbs and Persson, 1982). As the band of heavy precipitation passes over, the precipitation rate returns to the "background" stratiform rate.

Shown in Table 1 are comparisons between the precipitation rates derived from the present model calculations and the measurements described by Hobbs and Persson. Unfortunately, the core of heavy precipitation that Hobbs and Persson analyzed (for which the air motion pattern was computed and used as input in the present model studies) did not pass over a high-resolution tipping-bucket raingage on the Washington State coast. However, core 2 in Fig. 2 passed over Point Brown, where surface precipitation rates were measured. Since the radar measurements showed that cores 1 and 2 had similar structures, we assume they produced similar precipitation rates on the ground. Hence, in Table 1 the precipitation rates derived from the model simulations are compared with those measured in core 2. The average surface precipitation rate predicted by the model for the embedded case (9.0 mm h$^{-1}$) agrees well with the measured 10 min average precipitation rate of 8.0 mm h$^{-1}$. However, the peak surface precipitation rate predicted by the model (12.3 mm h$^{-1}$) is considerably lower than the measured 2 min average rate of 18.0 mm h$^{-1}$. This discrepancy could be due to differences between cores 1 and 2. However, since there is good agreement between the average precipitation rate derived from the model and the measured 10 min average value, the differences in the peak rates predicted by the model and the measurements might be due to the inability of the radar-derived air motion pattern to include smaller-scale cumulus motions that were present in both the updraft and downdraft regions (as evident from airborne measurements of the vertical velocity field discussed by Hobbs and Persson, 1982). Such small-scale, intense cumulus motions could produce small-scale precipitation maxima.

A cross section of the radar reflectivity values for the embedded simulation is shown in Fig. 14. Ahead of the updraft, in the stratiform region, the radar echo contours are oriented horizontally. However,

this stratification is disrupted in the updraft region. The maximum reflectivity of ~50 dB($Z$) at the 2.5 km level is produced by the accumulation of graupel at this level. Graupel falling to the surface is identifiable as a tilted shaft, where the reflectivities are ≥40 dB($Z$).

Another interesting feature in the model-computed reflectivity is an area of weaker radar reflectivity at low levels in the updraft region (between $x$ = 1.2 and $x$ = −2.4 km in Fig. 14), where the radar reflectivity is ~10 dB($Z$) less than the reflectivity at the same height in the stratiform region ahead of the updraft. It appears that the strength of the updraft prevents large precipitation particles from entering this region, either by horizontal advection or by falling vertically. The maximum snow mixing ratio in this region is only 0.01–0.05 g kg$^{-1}$ and there is no graupel. There is appreciable cloud water in this region (~0.6 g kg$^{-1}$), but the diameters of the droplets are assumed to be sufficiently small that they make a negligible contribution to the radar reflectivity. In fact, the radar reflectivity from cloud water alone (assuming a monodisperse diameter of 40 μm and $q_c$ = 0.6 g kg$^{-1}$) is only −10 dB($Z$). Browning and Harrold (1970) noted the presence of a weak-echo region within the updraft region of the narrow cold-frontal rainband they studied. This region was 1 to 2 km wide and the reflectivities were ~15 dB($Z$) weaker than the echoes at the same level ahead of the rainband, very similar to the situation modeled here. Browning and Harrold compared this weak-echo region to the "vault" region found in severe storms.

Also shown in Fig. 14 is the measured radar reflectivity pattern from the Hobbs and Persson case study (dashed lines). Only fair agreement is seen between this pattern and that produced by the model. For example, the field measurements do not show a region of high reflectivity near the 2.5 km level. In the model, this maximum in radar reflectivity was due to the accumulation of graupel within this region. Although the horizontal flow in this region was small, which contributed to the accumulation, the accumulation could have been unduly large as a result of relatively small mass-weighted fallspeeds of graupel. Values of $\bar{V}_g$ ranged from 2 to 2.5 m s$^{-1}$; if they had been larger, they would have likely lessened the accumulation of graupel in this area without significantly affecting the overall graupel distribution. When the graupel fallspeeds are uniformly increased by 1 m s$^{-1}$, the magnitude of the graupel content aloft decreases [with a peak reflectivity of 45 dB($Z$)] without significantly changing the location of the peak surface precipitation rate. It is suspected that increasing the fallspeeds even more would bring the predicted reflectivities into good agreement with the observations. We also note that the region of minimum reflectivity in the updraft region is less pronounced in the measurements than in the model results.

## 6. Sensitivity studies

### *a. Elimination of the vertical line source of snow $q_{s0}$*

In this section we test the sensitivity of various model outputs to the elimination of the vertical line source of snow $q_{s0}$. In this case the updraft/downdraft region associated with the narrow cold-frontal rainband is considered to be an isolated feature, independent of any surrounding precipitation. This will be referred to as the *nonembedded* simulation. In this case any graupel that forms must do so without the aid of ice particles entering the updraft region from surrounding stratiform clouds.

The model was initialized in the same manner as the embedded simulation, the only difference being that $q_{s0}$ = 0. The model was run until a steady state was achieved, which, as in the embedded simulation took approximately 3000 s.

The fields of temperature and water vapor condensation (PCOND) for the nonembedded simulation were virtually identical to those for the embedded simulation and they will not be discussed further. The cloud water content for the nonembedded simulation is shown in Fig. 15. Peak values of $q_c$ were 1.2 g kg$^{-1}$, somewhat larger than the maximum of 0.9 g kg$^{-1}$ for the embedded case (Fig. 7b).

Since the cloud water content is well above the threshold for autoconversion (PRAUT), rain can form in the updraft region. The autoconversion term and rain water mixing ratio are shown in Fig. 16. Autoconversion reaches peak values of nearly 5 × 10$^{-4}$ g kg$^{-1}$ s$^{-1}$, centered in the region of maximum cloud water content as expected (Fig. 16a). The rain mixing ratio above the 0°C level (located approximately 600 m above the surface) is peaked where autoconversion is a maximum. Although the values of $q_r$ are still relatively small (0.07 g kg$^{-1}$), they are over a factor of 2 larger than the maximum $q_r$ values in the embedded simulation (Fig. 10). The maximum in $q_r$ at the surface near $x$ = −4.8 km is again due to the presence of heavy precipitation (in the form of graupel above the 0°C level) that melts as it reaches the surface. Hence, graupel also forms in the nonembedded simulation. The following discussion

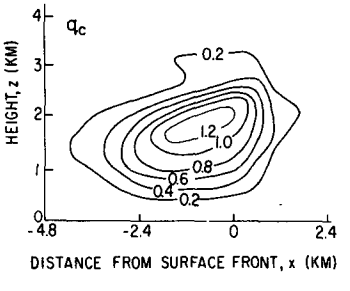


FIG. 15. Cloud water content $q_c$ for the nonembedded simulation. Units are g kg$^{-1}$.

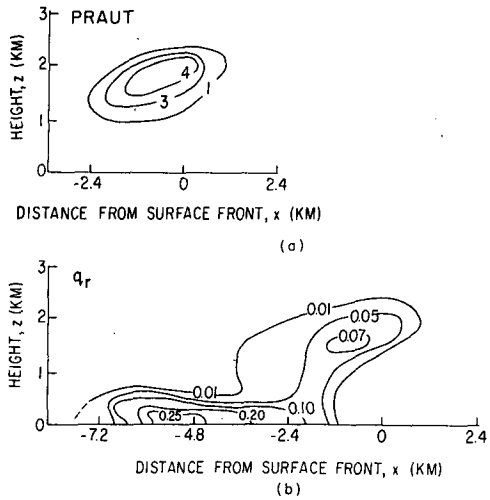


FIG. 16. Model results in the nonembedded simulation for (a) the initiation of rain by autoconversion (PRAUT), in units of $10^{-4}$ g kg$^{-1}$ s$^{-1}$, and (b) rainwater mixing ratios $q_r$ in units of g kg$^{-1}$.

provides details of the graupel-initiation process for this simulation and compares it with the embedded simulation.

The snow mixing ratio ($q_s$) for the nonembedded simulation is shown in Fig. 17. Snow first appears in the updraft region at approximately the −6°C level. The model contains three processes whereby snow can be initiated: conversion of cloud ice (PCONV), the Bergeron process (PSFI, PSFW), and the freezing of rain (PRACI, PIACR). The latter mechanism can also be a source for graupel if the rain mixing ratio exceeds 0.1 g kg$^{-1}$, but since this is not the case in the nonembedded simulation any frozen rain that might form contributes to snow, not graupel.

In the nonembedded simulation, the dominant mechanism for snow initiation is the freezing of rain (PRACI, PIACR). PIACR, the rate at which rain is transferred to snow due to freezing, is dominant and reaches peak values of $3 \times 10^{-5}$ g kg$^{-1}$ s$^{-1}$. PRACI, the rate at which cloud ice is transferred to snow, is at least $10^3$ times smaller than PIACR. This implies that the initial snow mass is dominated by frozen drops, rather than small cloud ice particles.

The two remaining snow initiation mechanisms are considerably smaller than PIACR. The conversion of cloud ice (PCONV) is zero throughout most of the updraft region and reaches values of $10^{-9}$ g kg$^{-1}$ s$^{-1}$ in the uppermost region of the updraft. The Bergeron terms (PSFI and PSFW) which represent, respectively, the transfer of cloud ice and cloud water to snow, are $\sim 10^{-7}$ g kg$^{-1}$ s$^{-1}$ near the top of the updraft region, at least two orders of magnitude smaller than PIACR.

Once snow is initiated by the drop freezing process, continued growth by riming (PSACW) is rapid, since the cloud water content is fairly large ($\sim$1 g kg$^{-1}$). Peak values of PSACW in the updraft region are $10^{-3}$ g kg$^{-1}$ s$^{-1}$ just below the 2 km level. The collection of rain by snow (PSACR) also contributes to the growth of snow but it is an order of magnitude less than PSACW. These are the only appreciable snow growth mechanisms.

Snow mixing ratios $\geq 0.1$ g kg$^{-1}$ are present at the 1.7 km level in the updraft (Fig. 17). Since at this level both snow and cloud water meet the threshold criteria for graupel initiation via riming (PSACW, PWACS), graupel can be produced.

The graupel distribution is shown in Fig. 18. The hatched area denotes the region where graupel is initiated by the riming of snow ("snow," in this case, consists of small frozen drops). Within this hatched region, the rate at which cloud water contributes to graupel (PSACW) is $10^{-3}$ g kg$^{-1}$ s$^{-1}$ and the rate at which snow is transferred to graupel (PWACS) is $10^{-2}$ g kg$^{-1}$ s$^{-1}$. The conversion of the snow to graupel produces a decrease in $q_s$ immediately above this level (Fig. 17). In this nonembedded simulation, the initiation of graupel occurs across the top portion of the updraft region, compared to the leading edge of the updraft region as in the embedded simulation.

Not only is there a difference in the graupel initiation region between the embedded and nonembedded simulations, but also distinct differences in the type of ice particles that serve as embryos for graupel. In the embedded simulation, the particles upon which graupel form are supplied by the stratiform cloud ahead of the narrow cold-frontal rainband; they therefore consist primarily of ice crystals grown from the

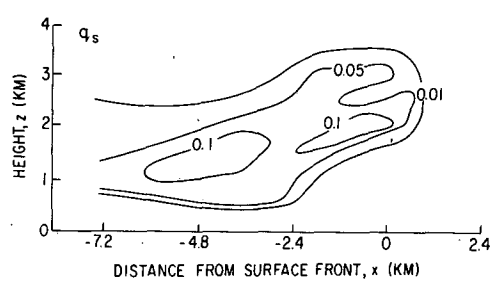


FIG. 17. The snow mixing ratio $q_s$ in the nonembedded simulation. Units of g kg$^{-1}$.

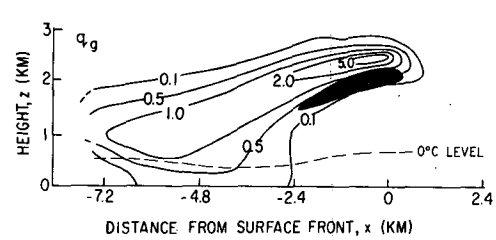


FIG. 18. The graupel mixing ratio $q_g$ in the nonembedded simulation. Units are g kg$^{-1}$. The hatched area denotes the region where graupel is initiated by snow accreting cloud water.

vapor phase and aggregates of these ice crystals. In the nonembedded simulation, graupel embryos are small, frozen raindrops.

The latter mechanism for forming graupel is similar to that modeled by Scott and Hobbs (1977) for a shallow maritime cumulus cloud. Their modeling results showed that droplets that form on large cloud condensation nuclei grow quickly and freeze when they collide with small ice crystals. These frozen drops continue to grow by riming and form graupel. In the nonembedded simulation, the autoconversion process produces rain, which, upon colliding with cloud ice (small ice crystals) and freezing, provides the initial particles that promote the development of graupel. Scott and Hobbs found from their explicit numerical model that 90 percent of the graupel particles originated on frozen drops. Although it is not possible to derive an analogous number from our parameterized model, the rate of snow initiation by drop freezing is at least $10^2$ times greater than the rate of snow initiation by either the conversion of cloud ice or the Bergeron process (in which cases snow would consist of crystals grown by deposition). Since graupel forms by the riming of snow, this implies that the bulk of the graupel present in the nonembedded simulation should also originate on frozen drops.

The similarities between the nonembedded case presented here, in which a parameterized model has been used, and the results of Scott and Hobbs, who used an explicit model, are reassuring since the isolated updraft–downdraft structure for the nonembedded simulation of a narrow cold-frontal rainband is similar to the isolated cumulus cell simulated by Scott and Hobbs.

Returning to Fig. 18, we see that the $q_g$ field for the nonembedded simulation is very similar to the $q_g$ field for the embedded simulation (Fig. 9), except for the lack of graupel at low levels in the updraft region. Graupel occurs at lower levels in the updraft region in the embedded simulation (1 km compared to 1.7 km in the nonembedded simulation) because it forms readily on the snow entering the updraft region from ahead of the front. In the nonembedded simulation, graupel cannot form until frozen drops have appeared,

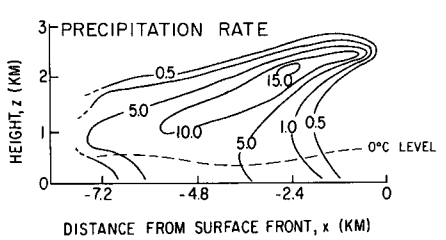


FIG. 19. The precipitation rate in the nonembedded simulation. Above the 0°C level the rate is the melted equivalent. Units are mm $h^{-1}$.

TABLE 2. Precipitation rates (mm $h^{-1}$) for the nonembedded and embedded model simulations. Also shown again for comparative purposes are the measured precipitation rates.

| | Model results | | Measurements | |
|---|---|---|---|---|
| Simulation | Peak* | Average** | Peak | Average |
| Nonembedded | 9.0 | 6.0 | | |
| Embedded | 12.3 | 9.0 | 18.0† | 8.0§ |

* Maximum precipitation rate at the surface.

** Average precipitation rate at the surface between $x = -2.4$ and $x = -7.2$ km during the passage of the narrow cold-frontal rainband.

† 2 min average precipitation rate from core 2.

§ 10 min average precipitation rate from core 2.

which first occurs at the 1.7 km level (−8°C). In both simulations there is a strong graupel maximum aloft and a sloping region of heavy graupel precipitation.

The growth of graupel in the nonembedded simulation is dominated by the accretion of cloud water (PGACW). This production term is very similar to PGACW in the embedded simulation (Fig. 11a) in both distribution in the $x$–$z$ plane and in magnitude. Other growth mechanisms for graupel are small compared to PGACW.

The precipitation rate is shown in Fig. 19 for the nonembedded simulation. Above the 0°C level the precipitation rate is due mainly to graupel (both $q_r$ and $q_s$ are much smaller than $q_g$). In this case, the precipitation rate ahead of the updraft region is zero since there is no input snow ($q_{s0}$). Since the mass-weighted fallspeeds of graupel (~2 m $s^{-1}$) are less than the magnitudes of the updrafts over a large region, graupel does not fall to the surface until it has been advected away from the updraft; this occurs approximately 2 km behind the surface front. The heaviest surface precipitation is found ~5 km to the rear of the updraft region, in the same location as the maximum surface precipitation in the embedded simulation.

A summary of the precipitation rates (both peak and average) is shown in Table 2 for both the nonembedded and embedded simulations, as well as measured values. There is a significant reduction in both the peak and average surface precipitation rates in the nonembedded simulation, both values are ~3 mm $h^{-1}$ less than in the embedded simulation.

The lower precipitation rates in the nonembedded simulation appear to be due to the lower removal of cloud water within the updraft region. (Peak values of $q_c$ were 1.2 g $kg^{-1}$ compared to peak values of 0.9 g $kg^{-1}$ in the embedded simulation.) Since the production rate for cloud water by condensation is virtually the same in both simulations, the presence of less cloud water in the embedded simulation implies that more was converted to precipitation. The greater removal of cloud water and hence higher

precipitation rates in the embedded simulation is due to the input of the ice particles into the updraft region from the stratiform clouds ahead of the narrow cold-frontal rainband.

In summary, the model results for the nonembedded simulation still show significant graupel precipitation. The graupel forms as follows. Rain is initiated by autoconversion due to the large values of cloud water in the updraft region. These drops freeze when they collide with cloud ice; this initiates the "snow" field. The snow particles continue to grow rapidly by accreting cloud water and are converted into graupel. In this sequence, the initial freezing of the rain triggers the rapid formation of graupel by providing centers onto which the graupel subsequently forms. However, precipitation rates are significantly less than for the embedded simulation.

### b. *Sensitivity to assumed threshold values for graupel initiation*

We now investigate the sensitivity of various model outputs in the embedded simulation to changes in the threshold values of rain, snow and cloud water required for graupel initiation. In the "standard case," discussed in the earlier section, it was assumed that if $q_s > 0.1$ g kg$^{-1}$ and $q_c > 0.5$ g kg$^{-1}$, graupel could be initiated by collisions between snow and cloud water. For graupel initiation by rain–snow collisions, it was assumed that both $q_r$ and $q_s$ had to be >0.1 g kg$^{-1}$. Similarly, for graupel initiation by rain–cloud ice collisions, it was assumed that $q_r$ had to be >0.1 g kg$^{-1}$ in the presence of cloud ice.

In the first sensitivity study that was performed, the threshold values of both $q_r$ and $q_s$ were lowered to 0.01 g kg$^{-1}$ and $q_c$ was lowered to 0.1 g kg$^{-1}$. Only minor changes occurred in various model outputs in this simulation. Graupel, initiated by the riming mechanism (snow–cloud water collisions), first appeared 2.5 km ahead of the surface front, compared with 1.2 km in the standard embedded simulation. Since lower cloud water contents were required for graupel initiation, graupel formed at a greater distance from the core of the updraft. However, since the bulk of the graupel mass was acquired in the main updraft region (where the bulk of the cloud water is located), the overall distribution of graupel remains unchanged. Furthermore, there was no change in the location of the peak surface precipitation rate.

In a second sensitivity study, the threshold values of $q_s$, $q_r$ and $q_c$ for graupel formation were raised to >1.0 g kg$^{-1}$. In this case, graupel did not form. Instead, snow from the stratiform clouds ahead of the rainband traverses the updraft region, increasing in mass by riming but remaining in the snow category. The snow mixing ratio (with peak values of 2 g kg$^{-1}$) exceeds the required threshold value for graupel initiation but $q_r$ and $q_c$ did not. The large threshold values assumed in this simulation are probably too restrictive.

Finally, we have tested the sensitivity of the model when graupel is not permitted to form by snow–cloud water collisions. In this simulation, graupel can only be initiated by collisions between snow and rain when both $q_s$ and $q_r$ are >0.1 g kg$^{-1}$, or by collisions between rain and cloud ice when $q_r$ is >0.1 g kg$^{-1}$. In this simulation, graupel does not form. As in the case when large threshold values were assumed, the input snow grows by accretion in the updraft region, but this accretional growth prevents the rain content from exceeding 0.1 g kg$^{-1}$, so graupel does not form.

In these latter two simulations the strong surface precipitation maximum located 5 km to the rear of the surface front is absent. When graupel does not form, the precipitation particles are snow which have slower fallspeeds. Hence these particles are carried to greater distances behind the surface front than were the graupel particles. During this transit the snow content undergoes greater dispersion which eliminates the narrow shaft of intense precipitation.

These sensitivity experiments illustrate the importance of collisions between snow and cloud water (i.e. riming) in the formation of graupel. Riming is not only vital to graupel formation in the narrow cold-frontal rainband, it dominates subsequent graupel growth as well.

### c. *Sensitivity to increases in the concentration of cloud ice*

We now examine the sensitivity of various model outputs in the embedded simulation to increases in the concentration of cloud ice. In the model, cloud ice consists of small nonprecipitating ice crystals. At initiation, the cloud ice crystals bear a one-to-one correspondence with the assumed ice nucleus concentrations specified by (Fletcher, 1962):

$$n_i = n_0 \exp[\beta(T_0 - T)], \tag{6}$$

where $n_i$ is the ice nucleus concentration, $T$ the temperature, $n_0 = 10^{-2}$ m$^{-3}$ and $T_0 = 273.16$.

It seems likely that an ice multiplication process was operating within the joint updraft–downdraft region in the narrow cold-frontal rainband studied by Hobbs and Persson (1982). This was indicated by the presence of larger concentrations of small ice crystals (<0.8 mm in diameter) within the updraft–downdraft region compared with the same level in the surrounding clouds. Hobbs and Persson suggested that ice splintering during the riming process was responsible for the production of these small ice crystals.

To approximate the effects of increased concentrations of small ice crystals that may result from an ice multiplication process (or from artificial seeding of the updraft region) several model runs were conducted

in which the concentrations of ice nuclei (and therefore small ice crystals) were given by (6) but with $n_0 = 10^{-1}$, 1 or 10 $m^{-3}$. These enhanced ice nucleus concentrations were confined to the circulation associated with the narrow cold-frontal rainband; they were not applied to the surrounding stratiform cloud.

With $n_0 = 10^{-1}$, there were only minor changes in the model outputs. This is because at the fairly high temperatures that existed in this rainband (the top of the updraft region was −12°C), increasing the ice nucleus concentration by a factor of 10 resulted in a cloud ice concentration of only 0.1 $L^{-1}$. This concentration was not sufficient to affect the cloud water field (that is, depositional growth of cloud ice as opposed to condensational growth of cloud droplets). Hence, the growth of graupel by the accretion of cloud water remained dominant.

More noticeable effects occurred with $n_0 = 1$ or 10 $m^{-3}$ in (6). In these simulations the concentrations of ice nuclei at the −12°C level were 1 and 10 $L^{-1}$ respectively. In these simulations a noticeable increase in the snow content ($q_s$) took place at and above the 3 km level in the updraft region. When $n_0 = 10^{-2}$ $m^{-3}$ or $10^{-1}$ $m^{-3}$, the snow content was generally 0.01–0.05 g $kg^{-1}$, whereas when higher values of $n_0$ were used, $q_s$ ranged from 0.1–0.3 g $kg^{-1}$. The larger values of $q_s$ at the top of the updraft region resulted due to the following process.

Larger ice nuclei concentrations resulted in larger values of cloud ice ($q_i$) through both initiation (PINT) and depositional growth (PDEPI). Hence, more condensate was removed by deposition onto cloud ice as opposed to condensation onto cloud droplets. (However, water saturated conditions were still maintained in this region.) Ultimately, these increases in cloud ice resulted in more snow production through the Bergeron process (PSFI, PSFW) at and above the 3 km level. PSFI (a sink for cloud ice) was $\sim 10^{-4}$ g $kg^{-1}$ $s^{-1}$ and PSFW (a sink for cloud water) was $\sim 10^{-5}$ g $kg^{-1}$ $s^{-1}$. Interestingly, the conversion of cloud ice to snow (PCONV), which corresponds to the production of snow when cloud ice exceeds a mean diameter of 500 μm was zero in this region. Apparently, the efficiency of the Bergeron process in producing snow reduces PCONV to zero.

The increased production of snow and loss of cloud water at and above the 3 km level in the updraft region had very little effect on the graupel content (and hence precipitation rate). The bulk of the graupel was confined below the 3 km level, since the mass-weighted fallspeed of the graupel exceeded the updraft velocities at and just below this level (the maximum in the $q_g$ field was at 2.3 km). Therefore, only minor graupel growth took place above the 3 km level. When $n_0$ was 1 or 10 $m^{-3}$, the graupel grew by collecting snow (PGACS $\sim 10^{-4}$ g $kg^{-1}$ $s^{-1}$) in this region, as opposed to collecting cloud water (PGACW $\sim 10^{-4}$ g $kg^{-1}$ $s^{-1}$) when lesser values of $n_0$ ($10^{-2}$ and $10^{-1}$ $m^{-3}$) were used. Since PGACS and PGACW were nearly the same in magnitude, both mechanisms contributed roughly the same graupel mass and the precipitation rate was unchanged.

The sensitivity studies indicate that the production of ice splinters during riming, as discussed by Hobbs and Persson (1982), may have had little effect on the production of precipitation within the narrow cold-frontal rainband. The splinters (or increased concentrations of small ice crystals) could be no more than a by-product of the precipitation process itself. Unless the small ice particles so produced can grow to appreciable sizes and begin to remove cloud water by riming in the short time they spend in the updraft region, there will be no appreciable changes in the precipitation from the rainband. However, the splinters could be important to precipitation formation in the stratiform cloud to the rear of the rainband since it is likely that they are advected into this region after detrainment from the top of the convective updraft. The results of these sensitivity studies should be viewed with caution since the high cloud ice concentrations were not a result of the riming process, but were simply increased by various assumed amounts in the region where splinter formation would be expected to occur.

### *d. Sensitivity to $q_{s0}$*

We now describe the sensitivity of the surface precipitation rate beneath the narrow cold-frontal rainband to changes in the precipitation rate in the stratiform region ahead of the updraft region. This study was conducted by changing the values of the input snow profile ($q_{s0}$) ahead of the narrow cold-frontal rainband.

The results are summarized in Table 3. The precipitation rate beneath the narrow cold-frontal rainband increases as $q_{s0}$ increases. For example, when

TABLE 3. Model results for the average and maximum surface precipitation rates at the surface (mm $h^{-1}$) and the maximum cloud water contents in the updraft region of the narrow cold-frontal rainband resulting from different input precipitation rates from the stratiform region ahead of the cold front.

| Precipitation rate in the stratiform region (mm $h^{-1}$) | Surface precipitation rate in the narrow cold-frontal rainband (mm $h^{-1}$) | | Maximum cloud water content (g $kg^{-1}$) |
|---|---|---|---|
| | Average | Maximum | |
| 10.0 | 19.0 | 23.0 | 0.6 |
| 5.0 | 14.0 | 16.0 | 0.8 |
| 1.0* | 9.0 | 12.0 | 0.9 |
| 0.5 | 8.0 | 10.0 | 1.0 |
| 0.0** | 6.0 | 8.0 | 1.2 |

* Standard embedded simulation.
** Nonembedded simulation.

$q_{s0}$ is an order of magnitude larger than the value in the "standard" embedded simulation (10.0 mm $h^{-1}$ compared to 1.0 mm $h^{-1}$), the peak precipitation rate increases from 12.0 to 23.0 mm $h^{-1}$. In all cases, the precipitation rate from the narrow cold-frontal rainband is greater when input snow from the stratiform region is included.

Also shown in Table 3 are the peak cloud water contents. These are largest when little or no snow enters the narrow cold-frontal rainband from the stratiform region, and they rapidly decrease as $q_{s0}$ is increased. Since the rate at which cloud water is produced by condensation is nearly the same in all cases, the lower values of $q_c$ are a consequence of the increased removal rates of cloud water through accretion by graupel. Hence, as $q_{s0}$ is increased, cloud water is removed more efficiently, resulting in larger precipitation rates.

### *e. Precipitation production by a warm-rain process*

Observational studies of narrow cold-frontal rainbands by Kessler and Wexler (1960)[3] and Hobbs *et al.* (1980) indicated that the precipitation can form by a warm-rain process, since the updraft–downdraft regions associated with the rainbands in these studies were located entirely below the 0°C level. We have therefore modeled the development of precipitation within the airflow pattern described by Hobbs and Persson (1982) assuming there was no ice. This was done by setting $n_0 = 0$ in (6) and eliminating the vertical line source of snow ahead of the rainband ($q_{s0} = 0$). This simulation is somewhat artificial, since the same initial temperature sounding was used as in the previous simulations. Furthermore, if a warmer sounding had been used, more water vapor would be available for condensation.

The model results for this case show the cloud water content achieving values in excess of the required threshold for autoconversion (PRAUT). Rain formed by this process grows rapidly by collection (PRACW), and heavy precipitation is produced on the ground. The maximum value of $q_r$ was 1.0 g $kg^{-1}$, located within the updraft between 1 and 2 km above the surface (Fig. 20a). The rainfall rates are shown in Fig. 20b. The peak rate at the surface is ~20 mm $h^{-1}$, nearly twice as large as the surface precipitation rate when graupel was the main form of precipitation. This peak rate occurs just 2.4 km to the rear of the surface front, compared with 5 km when graupel was the dominant form of precipitation. Since the mass-weighted fallspeed of the rain is ~6 m $s^{-1}$, compared with ~2 m $s^{-1}$ for the graupel, the rain reaches the surface nearer to the surface front.

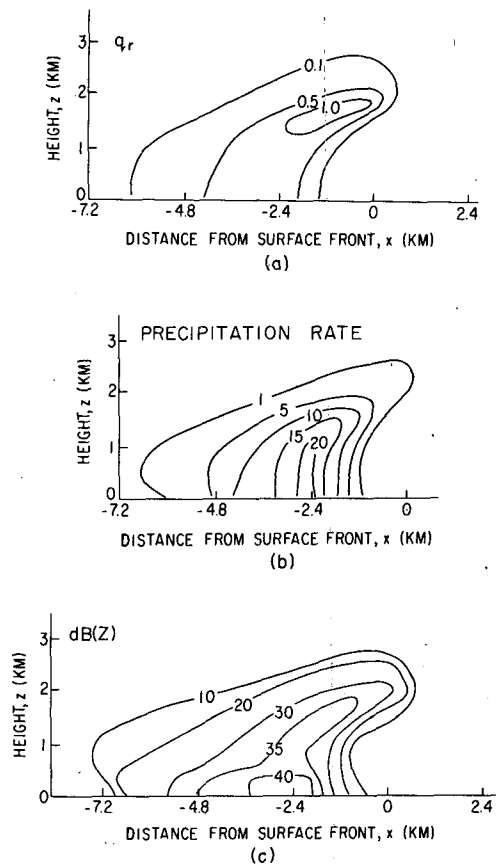


FIG. 20. Model results when the ice phase is excluded: (a) rainwater content $q_r$ in g $kg^{-1}$; (b) rainfall rate in mm $h^{-1}$; (c) radar reflectivity in dB(Z).

The high rainfall rate in this simulation results from the rain falling through more cloud of higher liquid water content than did the graupel particles. In the simulation discussed in Section 5, the graupel grew primarily as it moved upward through a region of high liquid water content; only small amounts of accretional growth occurred after the graupel exited the top of the updraft. As a result of the larger fallspeeds for rain, rain falls to the surface through the updraft region (which has high cloud water contents) and it grows rapidly by the collection of cloud water (PRACW).

The profiles of radar reflectivity for this model simulation are shown in Fig. 20c. The reflectivity profile is quite shallow, with the strongest echo (apart from the surface maximum) occurring just below 2 km, coincident with the region where $q_r$ is a maximum (Fig. 20a).

The sensitivity study suggests that warm-rain processes can produce substantial precipitation in cold fronts, provided that the updraft is sufficiently strong. However, this conclusion should again be viewed with caution because of the ease with which a param-

[3] Although narrow cold-frontal rainbands were not defined as such at the time of this study, the observational evidence presented indicates that the precipitation event was indeed a narrow cold-frontal rainband.

eterized model of the type used here produces precipitation by autoconversion and coalescence. The highly parameterized autoconversion process, which is responsible for initiating rain, greatly simplifies the processes involved in the evolution of a cloud droplet spectrum to produce rain.

## 7. Conclusions

In this paper we have described a diagnostic modeling study of the cloud and precipitation processes in narrow cold-frontal rainbands. The simulations consisted of an "embedded" simulation, where the prescribed air circulation associated with the rainband itself was assumed to be embedded within a region of stratiform precipitation, and a series of model sensitivity studies.

In the embedded simulation, the model indicates that graupel forms when ice particles from the stratiform region ahead of the narrow cold-frontal rainband enter the strong updraft region, where they grow rapidly by riming. Once formed, the graupel continues to grow by collecting cloud water. The model results for the cloud water content, surface precipitation rates and radar reflectivity are in reasonable agreement with field measurements.

If the source of ice particles from the stratiform region ahead of the narrow cold-frontal rainband is eliminated ("nonembedded" simulation), the model still predicts heavy graupel precipitation, but the sequence of microphysical processes leading to the initiation of graupel is quite different from the embedded simulation. In the nonembedded simulation, snow is first produced in the updraft region when rain (formed through the autoconversion of cloud water) freezes upon colliding with cloud ice. The snow then grows by riming to form graupel. Thus, the graupel embryos are frozen droplets, in contrast to the embedded simulation where the graupel embryos consisted of large ice crystals or aggregates. The precipitation rate from the rainband was larger in the embedded simulation due to the more efficient removal of cloud water in the updraft region as a result of the sweeping action of the ice particles flowing into the rainband from the stratiform region.

Additional sensitivity studies indicated that the snow–cloud water mechanism for initiating graupel, as opposed to rain–snow or rain–cloud ice collisions, is the only mechanism likely to initiate graupel in a narrow cold-frontal rainband. In another sensitivity study, the assumed ice nuclei concentrations were increased above those given by (6), to simulate the effect of ice multiplication. Although more snow was produced near the top of the updraft region at the expense of cloud water, no changes in the graupel content or precipitation rate resulted since the bulk of the graupel growth (by accreting cloud water) took place below the level where the cloud water content was lowered. A further sensitivity study indicated that heavy precipitation can possibly form in a narrow cold-frontal rainband through a warm-rain process. In this case, rain is initiated by autoconversion and grows rapidly by collecting cloud water, resulting in large precipitation rates.

The model results presented here are similar to the Type 2 simulations for warm-frontal rainbands discussed by Rutledge and Hobbs (1983). In these simulations, ice particles from weak convective clouds (the "seeder" zone) grew by collecting cloud water as they fell through a water-laden ("feeder") zone produced by strong, stable ascent. In a narrow cold-frontal rainband, surrounding stratiform cloud can act as a "seeder" zone by supplying ice particles that are fed into the updraft at the cold front, where they grow rapidly by riming. Therefore, in both warm-frontal and narrow cold-frontal rainbands, precipitation is produced most readily when stratiform and convective clouds operate in unison.

*Acknowledgments.* We thank J. Locatelli for many hours spent discussing model results as well as the reviewers whose comments were very constructive. This paper was written while one of us (P.V.H.) held a U.S. Senior Scientist Award from the Alexander von Humboldt Foundation at the Fraunhofer Institute für Atmosphärische Umweltforschung, Garmisch-Partenkirchen, FRG. This work was supported by the National Science Foundation (NSF) under Grant ATM-8009203 and by the Air Force Office of Scientific Research. Computing support was provided by the National Center for Atmospheric Research, which is sponsored by the NSF.

## APPENDIX A

## Model Adjustment to Include Graupel

The model used in this study is an extension of that used by Rutledge and Hobbs (1983, hereafter called RH). However, the model has been expanded to include graupel. Only the formulation required to include this additional field is discussed here. The parameterization of the cloud and precipitation processes for water vapor, cloud water, cloud ice, rain and snow may be found in RH.

### 1. Mass-weighted fallspeed

All graupel particles (at a particular gridpoint) are assumed to fall vertically at their mass-weighted fallspeed, which depends on the graupel content ($q_g$). This fallspeed is defined as

$$\bar{V}_G = \frac{\int_0^\infty N_{DG}(D_G)M(D_G)V_G(D_G)dD_G}{\int_0^\infty N_{DG}(D_G)M(D_G)dD_G}, \quad \text{(A1)}$$

where $M(D_G) = (\pi/6)\rho_G D_G^3$. The fallspeed-diameter relation (for lump graupel) is given by Locatelli and Hobbs (1974) as

$$V_G(D_G) = \bar{a} D_G^{\bar{b}} \left(\frac{p_0}{p}\right)^{0.4}. \quad \text{(A2)}$$

From (A2), (A1) and (1):

$$\bar{V}_G = \bar{a} \frac{\Gamma(4+\bar{b})}{6} \lambda_G^{-\bar{b}} \left(\frac{p_0}{p}\right)^{0.4}, \quad \text{(A3)}$$

where $\lambda_G$ is given by (2) in this paper.

## 2. Parameterization of the cloud physics processes

We first describe the parameterization of the graupel-initiation mechanisms. We then describe the parameterizations for graupel growth and destruction (melting).

### *a. Graupel initiation mechanisms*

#### 1) GRAUPEL INITIATION BY RAIN–CLOUD ICE COLLISIONS (PRACI, PIACR)

When rain and cloud ice collide in regions where $T < 0°C$ (P*RACI in Fig. 1), rain is assumed to freeze instantaneously and, depending on the mixing ratio of rain ($q_r$) can be a source for either snow or graupel. To transfer rain and cloud ice to snow or graupel requires two terms. PRACI gives the rate at which cloud ice is collected by rain and hence is a sink term for cloud ice. PIACR gives the rate at which rain is frozen due to collisions with cloud ice and is therefore a sink for rain. The sum of these two terms is a source for either snow or graupel.

The collection of cloud ice by rain (PRACI) is given by the continuous collection equation:

$$\frac{dM(D_R)}{dt} = \frac{\pi}{4} \rho D_R^2 V_R(D_R) \left(\frac{p_0}{p}\right)^{0.4} q_i E_{RI}, \quad \text{(A4)}$$

where $V_R(D_R)$ is given by RH (their A2). Multiplying (A4) by (1) applied to rain (replacing $G$ by $R$) and integrating over the rain size distribution yields

$$\text{PRACI} = \frac{\pi}{4} \rho q_i E_{RI} N_{0R} \left(\frac{p_0}{p}\right)^{0.4} \left[\frac{a_0\Gamma(3)}{\lambda_R^3} + \frac{a_1\Gamma(4)}{\lambda_R^4} + \frac{a_2\Gamma(5)}{\lambda_R^5} + \frac{a_3\Gamma(6)}{\lambda_R^6}\right]. \quad \text{(A5)}$$

The rate at which a cloud ice particle collides with raindrops (assumed to be uniformly distributed throughout the volume) is

$$\frac{dM_i}{dt} = \int_0^\infty E_{RI} \frac{\pi}{4} D_R^2 V_R(D_R) \rho_L \frac{\pi}{6} D_R^3 N_{DR} dD_R. \quad \text{(A6)}$$

The rate that cloud ice particles collide with rain in a given volume is found by multiplying (A6) by the number concentration of cloud ice $n_{ci} = \rho q_i / \bar{M}_i$, where $\bar{M}_i$ is the average mass of a cloud ice particle. Therefore,

$$\text{PIACR} = n_{ci} E_{RI} \frac{\pi^2}{24} \rho_L N_{0R} \left(\frac{p_0}{p}\right)^{0.4} \left[\frac{a_0\Gamma(6)}{\lambda_R^6} + \frac{a_1\Gamma(7)}{\lambda_R^7} + \frac{a_2\Gamma(8)}{\lambda_R^8} + \frac{a_3\Gamma(9)}{\lambda_R^9}\right]. \quad \text{(A7)}$$

#### 2) GRAUPEL INITIATION BY COLLISIONS BETWEEN RAIN AND SNOW (PSACR, PRACS)

When graupel is initiated by collisions between rain and snow (P*SACR in Fig. 1), two terms are again required for mass continuity. PSACR gives the rate at which snow collects rain and is therefore a sink term for rain. PRACS represents the rate at which rain collects snow and is therefore a sink term for snow.

These terms may be expressed as (Lin *et al.*, 1983)

$$\text{PSACR} = E_{SR}\pi^2 \rho_L |\bar{V}_S - \bar{V}_R| N_{0R} N_{0S} \left(\frac{p_0}{p}\right)^{0.4} \times \left[\frac{5}{\lambda_R^6 \lambda_S} + \frac{2}{\lambda_R^5 \lambda_S^2} + \frac{0.5}{\lambda_R^4 \lambda_S^3}\right] \quad \text{(A8)}$$

for snow collecting rain, and

$$\text{PRACS} = E_{SR}\pi^2 \rho_S |\bar{V}_R - \bar{V}_S| N_{0R} N_{0S} \left(\frac{p_0}{p}\right)^{0.4} \times \left[\frac{5}{\lambda_S^6 \lambda_R} + \frac{2}{\lambda_S^5 \lambda_R^2} + \frac{0.5}{\lambda_S^4 \lambda_R^3}\right] \quad \text{(A9)}$$

for rain collecting snow. When the conditions for graupel initiation by this mechanism are satisfied (i.e., both $q_r$ and $q_s$ are >0.1 g kg$^{-1}$), both PSACR and PRACS contribute to graupel. If these requirements are not met, snow grows by collecting rain (PSACR) and PRACS is not used. However, when $T \geq 0°C$, PRACS is a source term for rain (collection of melting snow).

#### 3) GRAUPEL INITIATION BY SNOW–CLOUD WATER COLLISIONS (PSACW, PWACS)

Two terms are also involved when graupel is initiated by collisions between snow and cloud water (P*SACW in Fig. 1). PSACW gives the rate at which snow collects cloud water. PWACS represents the loss of snow due to collisions with cloud water.

The PSACW is given by (A22) in RH. The PWACS term is derived using similar arguments to those applied above in the derivation of PIACR (A7) and it takes the form:

$$\text{PWACS} = \bar{n}_c E_{SC} \frac{\pi^2}{24} a'' \rho_S N_{0S} \left(\frac{p_0}{p}\right)^{0.4} \frac{\Gamma(6+b)}{\lambda_S^{6+b}}, \quad \text{(A10)}$$

where $\bar{n}_c = \rho q_c/\bar{M}_c$ is the cloud droplet concentration. Knowledge of the fallspeed-diameter relation for snow is required in the derivation of (A10); this is given by (A4) in RH. If the threshold values for graupel initiation are not met, snow grows by collecting cloud water (PSACW) and PWACS is not used.

*b. Sources and sinks for graupel*

Once graupel has been initiated by any of the above mechanisms, it can continue to grow by a variety of accretional processes and by deposition. Sink terms for graupel are nonzero only when $T \geq 0°C$ and they involve only melting processes.

1) COLLECTION OF CLOUD WATER BY GRAUPEL (PGACW)

When cloud water and graupel are present together in regions where $T < 0°C$, the collection of cloud water by graupel is computed. Dry growth is assumed, that is, all collected cloud water is frozen immediately. This parameterization follows from an application of the continuous collection equation and is of the form:

$$\text{PGACW} = \frac{\rho\pi\bar{a}q_c E_{GC} N_{0G}}{4}\left(\frac{p_0}{p}\right)^{0.4}\frac{\Gamma(\bar{b}+3)}{\lambda_G^{\bar{b}+3}}, \quad \text{(A11)}$$

which is similar to the form used by Lin *et al.*

2) COLLECTION OF CLOUD ICE BY GRAUPEL (PGACI)

The collection of cloud ice by graupel (PGACI) is analogous to (A11), except in this case, cloud ice ($q_i$) is the collected mass:

$$\text{PGACI} = \frac{\rho\pi\bar{a}q_i E_{GI} N_{0G}}{4}\left(\frac{p_0}{p}\right)^{0.4}\frac{\Gamma(\bar{b}+3)}{\lambda_G^{\bar{b}+3}}. \quad \text{(A12)}$$

3) COLLECTION OF RAIN BY GRAUPEL (PGACR)

When graupel and rain coexist in regions where $T < 0°C$, graupel is allowed to increase in mass by accreting rain (dry-growth is assumed). Since both graupel and rain have appreciable fallspeeds, the parameterization of this collection process can be formulated in the same manner as PSACR in (A8); it is of the form:

$$\text{PGACR} = E_{GR}\pi^2\rho_L|\bar{V}_G - \bar{V}_R|N_{0R}N_{0G}\left(\frac{p_0}{p}\right)^{0.4} \times\left[\frac{5}{\lambda_R^6\lambda_G} + \frac{2}{\lambda_R^5\lambda_G^2} + \frac{0.5}{\lambda_R^4\lambda_G^3}\right]. \quad \text{(A13)}$$

4) COLLECTION OF SNOW BY GRAUPEL (PGACS)

This term is analogous to PGACR, except in this case graupel collects snow:

$$\text{PGACS} = E_{GS}\pi^2\rho_S|\bar{V}_G - \bar{V}_S|N_{0S}N_{0G}\left(\frac{p_0}{p}\right)^{0.4} \times\left[\frac{5}{\lambda_S^6\lambda_G} + \frac{2}{\lambda_S^5\lambda_G^2} + \frac{0.5}{\lambda_S^4\lambda_G^3}\right]. \quad \text{(A14)}$$

5) DEPOSITIONAL GROWTH OF GRAUPEL (PGDEP)

When graupel exists in regions where $T < 0°C$ and ice supersaturation is present, the growth of graupel by vapor deposition is computed. The growth rate of a graupel particle by deposition is

$$\frac{dM(D_G)}{dt} = \frac{C(\bar{S}_i - 1)/\epsilon_0}{A'' + B''}F, \quad \text{(A15)}$$

where $A'' = (L_S/K_aT)(L_SM_w/R^*T - 1)$ and $B'' = R^*T/\chi M_w e_{si}$ are given by Pruppacher and Klett (1978). In (A15) $C$ is the capacitance of the ice crystal, which is dependent on geometrical shape, and $F$ is a ventilation factor. For a spherical graupel particle, $C = 2\pi\epsilon_0 D_G$ and the ventilation coefficient is assumed to be given by (Beard and Pruppacher 1971):

$$F = 0.78 + 0.31S_c^{1/3}R_e^{1/2} \quad \text{(A16)}$$

where $R_e = V_G(D_G)D_G\rho/\mu$. Substituting these values into (A15) and integrating over all graupel sizes yields

$$\text{PGDEP} = \frac{2\pi N_{0G}(\bar{S}_i - 1)}{A'' + B''}\left[\frac{0.78}{\lambda_G^2} + 0.31\left(\frac{\bar{a}\rho}{\mu}\right)^{1/2}\left(\frac{p_0}{p}\right)^{0.2}\frac{\Gamma(\bar{b}/2 + 5/2)}{\lambda_G^{\bar{b}/2+5/2}}\right]. \quad \text{(A17)}$$

6) MELTING OF GRAUPEL (PGMLT)

When $T \geq 0°C$ the melting of graupel is computed. This rate is developed in a similar manner to the PSMLT (melting of snow) term discussed by RH. Using (A23) in RH applied to graupel, where the ventilation coefficient $F$ is given by (A16) above, the melting rate of graupel is:

$$\text{PGMLT} = \frac{-2\pi}{L_f}K_a(T - T_0)N_{0G}\left[\frac{0.78}{\lambda_G^2} + 0.31\left(\frac{\bar{a}\rho}{\mu}\right)^{1/2}\left(\frac{p_0}{p}\right)^{0.2}\frac{\Gamma(\bar{b}/2 + 5/2)}{\lambda_G^{\bar{b}/2+5/2}}\right]. \quad \text{(A18)}$$

7) EVAPORATION OF MELTING GRAUPEL (PMLTGE)

When graupel melts in air that is below water saturation, water can evaporate from the surface of the particle. This term is similar to (A17), except in this case evaporation occurs from a liquid surface and is of the form:

$$\text{PMLTGE} = \frac{2\pi N_{0G}(S-1)}{A'+B'}\left[\frac{0.78}{\lambda_G^2} + 0.31\left(\frac{\bar{a}\rho}{\mu}\right)^{1/2}\left(\frac{p_0}{p}\right)^{0.2}\frac{\Gamma(\bar{b}/2+5/2)}{\lambda_G^{\bar{b}/2+5/2}}\right], \quad \text{(A19)}$$

where $A' = (L_v/K_aT)(L_vM_w/R^*T - 1)$ and $B' = R^*T/\chi M_w e_{sw}$ (Pruppacher and Klett, 1978).

8) SHEDDING OF ACCRETED WATER (PGSHR)

When $T \geq 0°C$, rain and cloud water collected by graupel cannot be frozen, therefore, it must be shed. Following Lin *et al.* (1983) we assume that the rate at which the collected water is shed from melting graupel is equal to the rate at which it is collected:

$$\text{PGSHR} = \text{PGACR} + \text{PGACW}. \quad \text{(A20)}$$

All water shed is assumed to contribute to rain. However, the water is assumed to remain in contact with the graupel particle for a sufficient time to allow the ice and water to achieve thermal equilibrium, thereby enhancing the melting rate. Parameterization of this effect is given below.

9) ENHANCEMENT OF THE MELTING OF GRAUPEL BY THE ACCRETION OF WATER (PGACWM, PGACRM)

The melting of graupel is enhanced by the accretion of cloud water and rain. This enhanced melting rate is derived from a direct application of the First Law of Thermodynamics. The increase in internal energy due to the accretion of liquid water is balanced by the heat of fusion required for the phase transformation from solid to liquid.

For graupel accreting rain when $T \geq 0°C$,

$$\text{PGACRM} = \frac{-c_w}{L_f}(T - T_0)(\text{PGACR}), \quad \text{(A21)}$$

where PGACRM is the enhanced melting rate resulting from the accretion of rain, and PGACR is given by (A13).

The enhanced melting of graupel due to the accretion of cloud water is of the form

$$\text{PGACWM} = -\frac{c_w}{L_f}(T - T_0)(\text{PGACW}), \quad \text{(A22)}$$

where PGACW is given by (A11). These formulations are similar to those used by Lin *et al.*

*c) Source terms for the water continuity variables*

Listed below are the source terms for each water continuity field used in the simulation of the narrow cold-frontal rainband. Those processes represented by the acronyms listed below that have not been derived above (such as PCOND, PSDEP, PREVP, etc.) are given in RH.

For water vapor ($q_v$):

$$S_v = -[\text{PCOND} + \text{PREVP} + \text{PSDEP} + \text{PMLTEV}(T \geq 0°C) + \text{PINT} + \text{PDEPI} + \text{PGDEP} + \text{PMLTGE}(T \geq 0°C)]. \quad \text{(A23)}$$

For cloud water ($q_c$):

$$S_c = \text{PCOND} + \text{PSMLTI}(T \geq 0°C) - \text{PRAUT} - \text{PRACW} - \text{PSACW} - \text{PGACW} - \text{PSFW}. \quad \text{(A24)}$$

For cloud ice ($q_i$):

$$S_i = \text{PDEPI} + \text{PINT} - \text{PSMLTI}(T \geq 0°C) - \text{PSACI} - \text{PCONV} - \text{PGACI} - \text{PRACI} - \text{PSFI}. \quad \text{(A25)}$$

For rain ($q_r$) in regions where $T \geq 0°C$:

$$S_r = \text{PRAUT} + \text{PRACW} + \text{PREVP} - \text{PGMLT} - \text{PSMLT} - \text{PGACRM} - \text{PGACWM} + \text{PSACW} + \text{PRACS} + \text{PGSHR} - \text{PGACR}. \quad \text{(A26)}$$

For rain in regions where $T < 0°C$:

$$S_r = \text{PRAUT} + \text{PRACW} + \text{PREVP} - \text{PGACR} - \text{PSACR} - \text{PIACR}. \quad \text{(A27)}$$

For snow ($q_s$) in regions where $T \geq 0°C$:

$$S_s = \text{PSMLT} - \text{PRACS} - \text{PGACS} + \text{PMLTEV}. \quad \text{(A28)}$$

For snow in regions where $T < 0°C$:

$$S_s = \text{PCONV} + \text{PSACI} + \text{PSDEP} - \text{PGACS} + \text{PSFW} + \text{PSFI} + \text{PRACI}(\delta_1) + \text{PIACR}(\delta_1) + \text{PSACR}(\delta_2) - \text{PRACS}(1-\delta_2) + \text{PSACW}(\delta_3) - \text{PWACS}(1-\delta_3). \quad \text{(A29)}$$

In (A30) the deltas ($\delta$) have the following meanings:

$$\delta_1 = \begin{cases} 0 & \text{if } q_r > 0.1 \text{ g kg}^{-1} \\ 1 & \text{otherwise,} \end{cases} \quad \text{(A30)}$$

$$\delta_2 = \begin{cases} 0 & \text{if } q_r \text{ and } q_s > 0.1 \text{ g kg}^{-1} \\ 1 & \text{otherwise,} \end{cases} \quad \text{(A31)}$$

$$\delta_3 = \begin{cases} 0 & \text{if } q_s > 0.1 \text{ g kg}^{-1} \text{ and } q_c > 0.5 \text{ g kg}^{-1} \\ 1 & \text{otherwise.} \end{cases} \quad \text{(A32)}$$

For graupel ($q_g$) in regions where $T \geq 0°C$:

$$S_g = \text{PGMLT} + \text{PGACRM} + \text{PGACWM} + \text{PGACS} + \text{PMLTGE}. \quad \text{(A33)}$$

For graupel in regions where $T < 0°C$:

$$S_g = \text{PGACW} + \text{PGACR} + \text{PGACI} + \text{PGACS} + \text{PGDEP} + \text{PRACI}(1 - \delta_1) + \text{PIACR}(1 - \delta_1) + \text{PSACR}(1 - \delta_2) + \text{PRACS}(1 - \delta_2) + \text{PSACW}(1 - \delta_3) + \text{PWACS}(1 - \delta_3). \quad \text{(A34)}$$

Similarly, the diabatic heating terms $S_h$ used in the thermodynamic energy equation [(6) in RH] are

$$S_h = \frac{L_f}{c_p}[\text{PGMLT} + \text{PSMLT} + \text{PGACWM} + \text{PGACRM} - \text{PSMLTI} - \text{PRACS}] + \frac{L_c}{c_p}[\text{PCOND} + \text{PREVP} + \text{PMLTEV} + \text{PMLTGE}] \quad \text{(A35)}$$

for regions where $T \geq 0°C$, and

$$S_h = \frac{L_f}{c_p}[\text{PSACW} + \text{PIACR} + \text{PSACR} + \text{PGACR} + \text{PGACW} + \text{PSFW}] + \frac{L_c}{c_p}[\text{PCOND} + \text{PREVP}] + \frac{L_s}{c_p}[\text{PGDEP} + \text{PSDEP} + \text{PDEPI} + \text{PINT}] \quad \text{(A36)}$$

for regions where $T < 0°C$.

## APPENDIX B

### List of Symbols

| Symbol | Description | Value | SI units |
|---|---|---|---|
| $A'$ | Thermodynamic term | | m s kg$^{-1}$ |
| $A''$ | Thermodynamic term | | m s kg$^{-1}$ |
| $\bar{a}$ | Constant in fallspeed relation for graupel | 19.3 | m$^{(1-\bar{b})}$ s$^{-1}$ |
| $a''$ | Constant in fallspeed relation for snow | 1.139 | m$^{(1-b)}$ s$^{-1}$ |
| $a_0$ | Coefficient in polynomial fallspeed relation for rain | −0.267 | m s$^{-1}$ |
| $a_1$ | Coefficient in polynomial fallspeed relation for rain | $5.15 \times 10^3$ | s$^{-1}$ |
| $a_2$ | Coefficient in polynomial fallspeed relation for rain | $-1.0225 \times 10^6$ | m$^{-1}$ s$^{-1}$ |
| $a_3$ | Coefficient in polynomial fallspeed relation for rain | $7.55 \times 10^7$ | m$^{-2}$ s$^{-1}$ |
| $B'$ | Thermodynamic term | | m s kg$^{-1}$ |
| $B''$ | Thermodynamic term | | m s kg$^{-1}$ |
| $\bar{b}$ | Fallspeed exponent for graupel | 0.37 | |
| $b$ | Fallspeed exponent for snow | 0.11 | |
| $C$ | Capacitance of ice crystal | | F |
| $c_p$ | Specific heat of air at constant pressure | $1.005 \times 10^3$ | J kg$^{-1}$ K$^{-1}$ |
| $c_w$ | Specific heat of liquid water at 0°C | 4218 | J kg$^{-1}$ K$^{-1}$ |
| $D_G$ | Graupel diameter | | m |
| $D_R$ | Raindrop diameter | | m |
| $D_S$ | Snowflake diameter | | m |
| dB($Z_R$) | 10 log$_{10}$ (radar reflectivity factor for rain) | | |
| dB($Z_I$) | 10 log$_{10}$ (radar reflectivity factor for ice) | | |
| $E_{GC}$ | Graupel/cloud water collection efficiency | 1 | |
| $E_{GI}$ | Graupel/cloud ice collection efficiency | 0.1 | |
| $E_{GR}$ | Graupel/rain collection efficiency | 1 | |
| $E_{GS}$ | Graupel/snow collection efficiency | 0.1 | |
| $E_{RI}$ | Rain/cloud ice collection of efficiency | 1 | |
| $E_{SR}$ | Snow/rain collection efficiency | 1 | |
| $e_{si}$ | Saturation vapor pressure for ice | | N m$^{-2}$ |
| $e_{sw}$ | Saturation vapor pressure for water | | N m$^{-2}$ |
| $F$ | Ventilation factor for rain and graupel | | |
| $K_a$ | Thermal conductivity of air | $2.43 \times 10^{-2}$ | J m$^{-1}$ s$^{-1}$ K$^{-1}$ |
| $L_f$ | Latent heat of fusion | $3.34 \times 10^5$ | J kg$^{-1}$ |
| $L_s$ | Latent heat of sublimation | $2.5 \times 10^6$ | J kg$^{-1}$ |
| $L_v$ | Latent heat of condensation | $2.25 \times 10^6$ | J kg$^{-1}$ |
| $\bar{M}_c$ | Average mass of cloud droplet | $4 \times 10^{-12}$ | kg |
| $M_G$ | Mass of graupel per unit volume of air | | kg m$^{-3}$ |

APPENDIX B (*Continued*)

**List of Symbols**

| Symbol | Description | Value | SI units |
|---|---|---|---|
| $\bar{M}_I$ | Average mass of cloud ice particle | $6 \times 10^{-12}$ | kg |
| $M_R$ | Mass of rain per unit volume of air | | kg m$^{-3}$ |
| $M_S$ | Mass of snow per unit volume of air | | kg m$^{-3}$ |
| $M_W$ | Molecular weight of water | 18.0160 | |
| $M(D_G)$ | Mass of graupel particle of diameter $D_G$ | | kg |
| $M(D_R)$ | Mass of raindrop of diameter $D_R$ | | kg |
| $M(D_S)$ | Mass of snowflake of diameter $D_S$ | | kg |
| $N_{DG}dD_G$ | Number concentration of graupel particles with diameters between $D_G$ and $D_G + dD_G$ | | m$^{-3}$ |
| $N_{DR}dD_R$ | Number concentration of raindrops with diameters between $D_R$ and $D_R + dD_R$ | | m$^{-3}$ |
| $N_{DS}dD_S$ | Number concentration of snowflakes with diameters between $D_S$ and $D_S + dD_S$ | | m$^{-3}$ |
| $N_{0G}$ | Intercept value in graupel size distribution | $4 \times 10^6$ | m$^{-4}$ |
| $N_{0R}$ | Intercept value in raindrop size distribution | $8 \times 10^6$ | m$^{-4}$ |
| $N_{0S}$ | Intercept value in snowflake size distribution | $4 \times 10^6$ | m$^{-4}$ |
| $n_{ci}$ | Number concentration of cloud ice crystals | | m$^{-3}$ |
| $\bar{n}_c$ | Number concentration of cloud water droplets | | m$^{-3}$ |
| $n_i$ | Number concentration of ice nuclei | | m$^{-3}$ |
| $n_0$ | Constant in expression for ice nuclei concentration | variable | m$^{-3}$ |
| $p$ | Pressure | | N m$^{-2}$ |
| $p_0$ | Constant in empirical relation | $10^6$ | N m$^{-2}$ |
| PCOND | Condensation of water vapor | | kg m$^{-3}$ s$^{-1}$ |
| PCONV | Conversion of cloud ice to snow | | kg m$^{-3}$ s$^{-1}$ |
| PDEPI | Depositional growth of cloud ice | | kg m$^{-3}$ s$^{-1}$ |
| PSFI | Conversion of cloud ice to snow in the Bergeron process | | kg m$^{-3}$ s$^{-1}$ |
| PSFW | Conversion of cloud water to snow in the Bergeron process | | kg m$^{-3}$ s$^{-1}$ |
| PGACI | Collection of cloud ice by graupel | | kg m$^{-3}$ s$^{-1}$ |
| PGACR | Collection of rain by graupel | | kg m$^{-3}$ s$^{-1}$ |
| PGACRM | Enhanced melting of graupel due to accretion of rain | | kg m$^{-3}$ s$^{-1}$ |
| PGACS | Collection of snow by graupel | | kg m$^{-3}$ s$^{-1}$ |
| PGACW | Collection of cloud water by graupel | | kg m$^{-3}$ s$^{-1}$ |
| PGACWM | Enhanced melting of graupel due to accretion of cloud water | | kg m$^{-3}$ s$^{-1}$ |
| PGDEP | Depositional growth of graupel | | kg m$^{-3}$ s$^{-1}$ |
| PGMLT | Melting of graupel | | kg m$^{-3}$ s$^{-1}$ |
| PGSHR | Shedding of accreted water by graupel | | kg m$^{-3}$ s$^{-1}$ |
| PIACR | Collection of rain by cloud ice | | kg m$^{-3}$ s$^{-1}$ |
| PINT | Initiation of cloud ice | | kg m$^{-3}$ s$^{-1}$ |
| PMLTEV | Evaporation of melting snow | | kg m$^{-3}$ s$^{-1}$ |
| PMLTGE | Evaporation of melting graupel | | kg m$^{-3}$ s$^{-1}$ |
| PRACI | Collection of cloud ice by rain | | kg m$^{-3}$ s$^{-1}$ |
| PRACS | Collection of snow by rain | | kg m$^{-3}$ s$^{-1}$ |
| PRACW | Collection of cloud water by rainwater | | kg m$^{-3}$ s$^{-1}$ |
| PRAUT | Autoconversion of cloud water | | kg m$^{-3}$ s$^{-1}$ |
| PREVP | Evaporation of rainwater | | kg m$^{-3}$ s$^{-1}$ |
| PSACI | Collection of cloud ice by snow | | kg m$^{-3}$ s$^{-1}$ |
| PSACR | Collection of rain by snow | | kg m$^{-3}$ s$^{-1}$ |
| PSACW | Collection of cloud water by snow | | kg m$^{-3}$ s$^{-1}$ |
| PSDEP | Depositional growth of snow | | kg m$^{-3}$ s$^{-1}$ |
| PSMLT | Melting of snow | | kg m$^{-3}$ s$^{-1}$ |

APPENDIX B (*Continued*)

**List of Symbols**

| Symbol | Description | Value | SI units |
|---|---|---|---|
| PSMLTI | Melting of cloud ice | | kg $m^{-3}$ $s^{-1}$ |
| PWACS | Collection of snow by cloud water | | kg $m^{-3}$ $s^{-1}$ |
| $q_c$ | Mixing ratio of cloud water | | kg $kg^{-1}$ |
| $q_g$ | Mixing ratio of graupel | | kg $kg^{-1}$ |
| $q_i$ | Mixing ratio of cloud ice | | kg $kg^{-1}$ |
| $q_r$ | Mixing ratio of rain water | | kg $kg^{-1}$ |
| $q_s$ | Mixing ratio of snow | | kg $kg^{-1}$ |
| $q_{s0}$ | Mixing ratio of input snow | | kg $kg^{-1}$ |
| $q_v$ | Mixing ratio of water vapor | | kg $kg^{-1}$ |
| $R^*$ | Universal gas constant | $8.314 \times 10^3$ | J $kmol^{-1}$ $K^{-1}$ |
| $R_e$ | Reynolds number | | |
| $R_w$ | Gas constant for water vapor | $4.61 \times 10^2$ | J $kg^{-1}$ $K^{-1}$ |
| $S$ | Saturation ratio with respect to water | | |
| $S_c$ | Schmidt number | 0.6 | |
| $S_c$ | Source term for cloud water | | kg $m^{-3}$ $s^{-1}$ |
| $S_h$ | Diabatic heating terms | | K kg $m^{-3}$ $s^{-1}$ |
| $S_i$ | Source term for cloud ice | | kg $m^{-3}$ $s^{-1}$ |
| $S_i$ | Saturation ratio with respect to ice | | |
| $S_0$ | Represents sources and sinks for $q$ | | kg $m^{-3}$ $s^{-1}$ |
| $S_g$ | Source term for graupel | | kg $m^{-3}$ $s^{-1}$ |
| $S_r$ | Source term for rain | | kg $m^{-3}$ $s^{-1}$ |
| $S_s$ | Source term for snow | | kg $m^{-3}$ $s^{-1}$ |
| $S_v$ | Source term for water vapor | | kg $m^{-3}$ $s^{-1}$ |
| $T$ | Temperature | | K |
| $T_0$ | Reference temperature | 273.16 | K |
| $t$ | Time | | s |
| $u$ | Horizontal windspeed | | m $s^{-1}$ |
| $\bar{V}$ | Mass-weighted fallspeed of precipitation | | m $s^{-1}$ |
| $\bar{V}_G$ | Mass-weighted fallspeed for graupel | | m $s^{-1}$ |
| $V_G(D_G)$ | Fallspeed of graupel particle of diameter $D_G$ | | m $s^{-1}$ |
| $\bar{V}_R$ | Mass-weighted fallspeed for rain | | m $s^{-1}$ |
| $V_R(D_R)$ | Fallspeed of raindrop of diameter $D_R$ | | m $s^{-1}$ |
| $\bar{V}_S$ | Mass-weighted fallspeed for snow | | m $s^{-1}$ |
| $V_S(D_S)$ | Fallspeed of snowflake of diameter $D_S$ | | m $s^{-1}$ |
| $w$ | Vertical air velocity | | m $s^{-1}$ |
| $x$ | Horizontal distance | | m |
| $Z$ | Equivalent radar reflectivity factor | | $mm^6$ $m^{-3}$ |
| $z$ | Vertical distance | | m |
| $\beta$ | Constant in ice crystal concentration | 0.6 | $K^{-1}$ |
| $\Gamma$ | Gamma function | | |
| $\Gamma_d$ | Dry adiabatic lapse rate | $9.8 \times 10^{-3}$ | K $m^{-1}$ |
| $\epsilon_0$ | Permittivity of free space | $8.854 \times 10^{-12}$ | $C^2$ $N^{-1}$ $m^{-2}$ |
| $\rho$ | Air density | | kg $m^{-3}$ |
| $\rho_G$ | Density of graupel | 400 | kg $m^{-3}$ |
| $\rho_L$ | Density of water | $10^3$ | kg $m^{-3}$ |
| $\rho_S$ | Density of snow | 100 | kg $m^{-3}$ |
| $\lambda_G$ | Slope of graupel size distribution | | $m^{-1}$ |
| $\lambda_R$ | Slope of raindrop size distribution | | $m^{-1}$ |
| $\lambda_S$ | Slope of snow size distribution | | $m^{-1}$ |
| $\chi$ | Diffusivity of water vapor in air | $2.26 \times 10^{-5}$ | $m^2$ $s^{-1}$ |
| $\mu$ | Dynamic viscosity of air | $1.718 \times 10^{-5}$ | kg $m^{-1}$ $s^{-1}$ |
| $\Delta t$ | Time increment | 10 | s |
| $\Delta x$ | Horizontal spatial increment | 600 | m |
| $\Delta z$ | Vertical spatial increment | 150 | m |

## REFERENCES


Beard, K. V., and H. R. Pruppacher, 1971: A wind tunnel investigation of the rate of evaporation of small water droplets falling at terminal velocity in air. *J. Atmos. Sci.*, **28,** 1455–1464.

Browning, K. A., and T. W. Harrold, 1970: Air motion and precipitation growth at a cold front. *Quart. J. Roy. Meteor. Soc.*, **96,** 369–389.

Carbone, R. E., 1982: A severe winter squall line. Part I: Stormwide hydrodynamic structure. *J. Atmos. Sci.*, **39,** 258–279.

Fletcher, N. H., 1962: *The Physics of Rainclouds.* Cambridge University Press, 386 pp.

Herzegh, P. H., and P. V. Hobbs, 1980: The mesoscale and microscale structure and organization of clouds and precipitation in midlatitude cyclones. II: Warm-frontal clouds. *J. Atmos. Sci.*, **37,** 597–611.

——, and ——, 1981: The mesoscale and microscale structure and organization of clouds and precipitation in midlatitude cyclones. IV: Vertical air motions and microphysical structures of prefrontal surge clouds and cold-frontal clouds. *J. Atmos. Sci.*, **38,** 1771–1784.

Hobbs, P. V., 1978: Organization and structure of clouds and precipitation on the mesoscale and microscale in cyclonic storms. *Rev. Geophys. Space Phys.*, **16,** 741–755.

——, and K. R. Biswas, 1979: The cellular structure of narrow cold-frontal rainbands. *Quart. J. Roy. Meteor. Soc.*, **105,** 723–727.

——, and P. O. G. Persson, 1982: The mesoscale and microscale structure and organization of clouds and precipitation in midlatitude cyclones. Part V: The substructure of narrow cold-frontal rainbands. *J. Atmos. Sci.*, **39,** 280–295.

——, T. J. Matejka, P. H. Herzegh, J. D. Locatelli and R. A. Houze, Jr., 1980: The mesoscale and microscale structure and organization of clouds and precipitation in midlatitude cyclones. I: A case study of a cold front. *J. Atmos. Sci.*, **37,** 568–596.

Houze, R. A., Jr., P. V. Hobbs, P. H. Herzegh and D. B. Parsons, 1979: Size distributions of precipitation particles in frontal clouds. *J. Atmos. Sci.*, **36,** 156–162.

——, S. A. Rutledge, T. J. Matejka and P. V. Hobbs, 1981: The mesoscale and microscale structure and organization of clouds and precipitation in midlatitude cyclones. III: Air motions and precipitation growth in a warm-frontal rainband. *J. Atmos. Sci.*, **38,** 639–649.

James, P. K., and K. A. Browning, 1979: Mesoscale structure of line convection at surface cold fronts. *Quart. J. Roy. Meteor. Soc.*, **105,** 371–382.

Jonas, P. R., and R. C. Tabony, 1973: Precipitation growth at a cold front. *Quart. J. Roy. Meteor. Soc.*, **99,** 252–259.

Kessler, E., III, and R. Wexler, 1960: Observations of a cold front, 1 October 1958. *Bull. Amer. Meteor. Soc.*, **41,** 253–257.

Lin, Y-L., R. D. Farley and H. D. Orville, 1983: Bulk parameterization of the snow field in a cloud model. *J. Climate Appl. Meteor.*, **22,** 1065–1092.

Locatelli, J. D., and P. V. Hobbs, 1974: Fallspeeds and masses of solid precipitation particles. *J. Geophys. Res.*, **79,** 2185–2197.

Marshall, J. S., and W. M. Palmer, 1948: The distribution of raindrops with size. *J. Meteor.*, **5,** 165–166.

Matejka, T. J., R. A. Houze, Jr. and P. V. Hobbs, 1980: Microphysics and dynamics of clouds associated with mesoscale rainbands in extratropical cyclones. *Quart. J. Roy. Meteor. Soc.*, **106,** 29–56.

Parsons, D. B., and P. V. Hobbs, 1983a: The mesoscale and microscale structure and organization of clouds and precipitation in midlatitude cyclones. VII: Formation, development, interaction and dissipation of rainbands. *J. Atmos. Sci.*, **40,** 559–579.

——, and ——, 1983b: The mesoscale and microscale structure and organization of clouds and precipitation in midlatitude cyclones. IX: Some effects of orography on rainbands. *J. Atmos. Sci.*, **40,** 1930–1949.

Pruppacher, H. R., and J. D. Klett, 1978: *Microphysics of Clouds and Precipitation.* Reidel, 714 pp.

Rutledge, S. A., and P. V. Hobbs, 1983: The mesoscale and microscale structure and organization of clouds and precipitation in midlatitude cyclones. VIII: A model for the "seeder-feeder" process in warm-frontal rainbands. *J. Atmos. Sci.*, **40,** 1185–1206.

Scott, B. C., and P. V. Hobbs, 1977: A theoretical study of the evolution of mixed phase cumulus clouds. *J. Atmos. Sci.*, **34,** 812–86.

Wang, P.-Y., D. B. Parsons and P. V. Hobbs, 1983: The mesoscale and microscale structure and organization of clouds and precipitation in midlatitude cyclones. VI: Wavelike rainbands associated with a cold-frontal zone. *J. Atmos. Sci.*, **40,** 543–558.